Search for New Particles Decaying to Two-jets with the DØ Detector

Iain A. Bertram
Northwestern University, Evanston, Illinois 60208

(January 31, 1997)

Results from a peliminary search for new particles decaying to dijets using the Run IA and IB data samples (104 pb^{-1}) are presented. We exclude at the 95% confidence level the production of excited quarks with masses below 725 GeV, an additional standard model W boson with masses between 340 and 680 GeV, an additional standard model Z boson with masses between 365 and 615 GeV and technirhos with masses between 230 and 700 GeV.

I. INTRODUCTION

The production of hadronic jets is the dominant contribution to high transverse momentum (p_T) processes in proton–antiproton ($\overline{p}p$) collisions. High p_T jets were observed in the early phase of experimentation at the CERN ISR and $\overline{p}p$ collider and their production properties are well described by perturbative QCD [1]. Although the Standard Model does an excellent job, there are many extensions of the Standard Model that predict the existence of new massive objects (e.g. excited quarks, W', Z', etc. [2,3]) which couple to quarks and gluons and will form resonant structures in the dijet mass spectrum. This paper will report on the search for these resonances in the dijet mass spectrum using the DØ detector. The observation of W and Z bosons decaying to two–jets by the UA2 experiment [4] displays the feasibility of dijet mass spectroscopy at $\overline{p}p$ colliders. Subsequently the UA2 [5] and CDF [6] experiments have searched for resonances in the dijet mass spectrum and produced limits on several different theoretical models.

II. DATA SAMPLE

The data sample used in this analysis was collected during 1992–93 and 1994–95 and corresponds to an integrated luminosity of 104.4 pb^{-1}. During the 1994–95 data taking period the data was collected using four triggers with E_T thresholds of 30, 50, 85 and 115 GeV with integrated luminosities of 0.36, 4.6, 52 and 91 pb^{-1}. These luminosities have an additional correction factor determined by matching the inclusive jet cross section in the region where two neighbouring triggers overlap. These corrections are 0.0±0.0, 2.8±1.3%, 5.7±1.5%, and 6.3±1.6% for the four 1994–95 data sets respectively [8]. Only one trigger was used from the 1992–93 data taking period with an E_T threshold of 115 GeV and an integrated luminosity of 13.7 pb^{-1}. The standard jet quality cuts (a complete description of these cuts can be found in references [7,8]) and the energy corrections are applied to the data .

Assuming that the individual jets are massless, the dijet mass is given by:

$$M_{jj}^2 = 2 \cdot E_{T_1} \cdot E_{T_2} \cdot (\cosh(\Delta\eta) - \cos(\Delta\phi)) \tag{2.1}$$

where E_{T_1} and E_{T_2} are the transverse energies of two jets with the highest E_T. Each event is weighted by $1/\epsilon$ where ϵ is the efficiency of the jet quality cuts [9] applied to the data. Cuts are then made to restrict the two leading jets to a region of the detector where jets are well measured and the the triggers are fully efficient:

$$\begin{aligned} |\eta_{1,2}| &< 1.0 \\ \Delta\eta = |\eta_1 - \eta_2| &< 1.6 \\ M_{jj} &> 200 \text{ GeV} \end{aligned} \tag{2.2}$$

The cut on the η of the two leading jets are applied to contain the jets in a region where the jet energy scale is well understood and to maximize the signal to noise (heavy objects will decay more centrally than QCD dijet production). The cut on $\Delta\eta$ is used to improve the acceptance of the triggers being used in the analysis [1].

[1]For example without the $\Delta\eta$ cut we would only be able to use the Jet_Max filter for $M_{jj} > 530$ GeV.

The four triggers (E_T thresholds of 30, 50, 85 and 115 GeV) where used above mass thresholds of 200, 270, 370 and 500 GeV were each of the triggers is 100% efficient. The resulting mass spectrum is depicted in Fig 1 (see table I for a full description of the data used in this analysis).

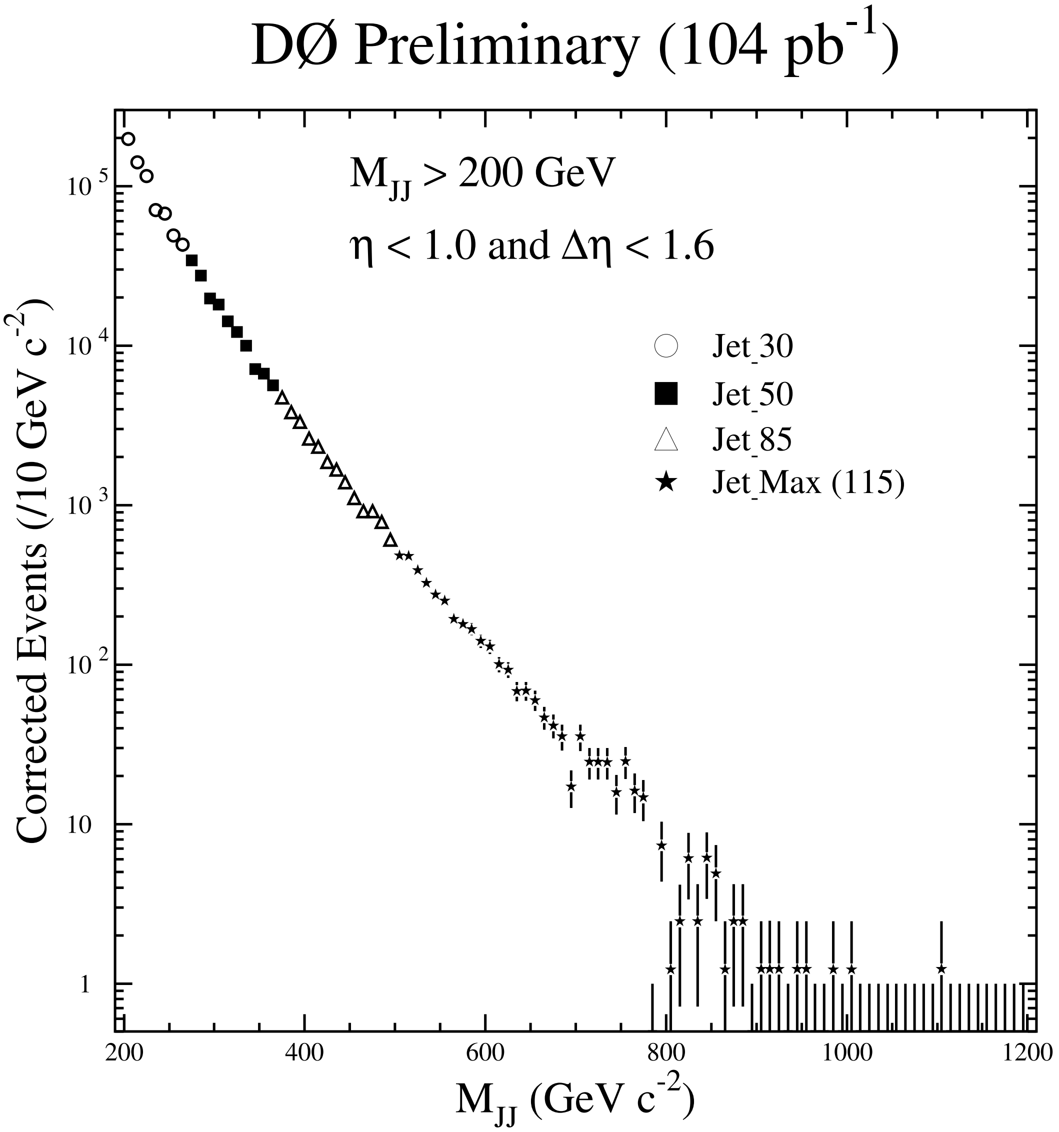

FIG. 1. The inclusive dijet mass spectrum. The events from each trigger have been corrected by the trigger's luminosity, event weights and vertex efficiency.

TABLE I. Data Used in this analysis for the nominal energy corrections (Note that the luminosities have been corrected by the appropriate correction factors (see section II)).

$M_{jj_{min}}$	$M_{jj_{max}}$	Number of Events	Event Weight	Vertex Efficiency	Luminosity
200	210	507	1.0733	89.29 $\pm$ 0.13	0.34
210	220	360	1.0752	89.29 $\pm$ 0.13	0.34
220	230	296	1.0771	89.29 $\pm$ 0.13	0.34
230	240	181	1.0797	89.29 $\pm$ 0.13	0.34
240	250	171	1.0813	89.29 $\pm$ 0.13	0.34
250	260	125	1.0832	89.29 $\pm$ 0.13	0.34
260	270	109	1.0846	89.29 $\pm$ 0.13	0.34
270	280	1187	1.0853	89.36 $\pm$ 0.08	4.56
280	290	955	1.0868	89.36 $\pm$ 0.08	4.56
290	300	687	1.0878	89.36 $\pm$ 0.08	4.56
300	310	627	1.0883	89.36 $\pm$ 0.08	4.56
310	320	490	1.0895	89.36 $\pm$ 0.08	4.56
320	330	422	1.0904	89.36 $\pm$ 0.08	4.56
330	340	344	1.0907	89.36 $\pm$ 0.08	4.56
340	350	246	1.0911	89.36 $\pm$ 0.08	4.56
350	360	230	1.0918	89.36 $\pm$ 0.08	4.56
360	370	195	1.0934	89.36 $\pm$ 0.08	4.56
370	380	2115	1.0929	90.35 $\pm$ 0.04	56.48
380	390	1709	1.0936	90.35 $\pm$ 0.04	56.48
390	400	1492	1.0947	90.35 $\pm$ 0.04	56.48
400	410	1174	1.0942	90.35 $\pm$ 0.04	56.48
410	420	1040	1.0954	90.35 $\pm$ 0.04	56.48
420	430	836	1.0961	90.35 $\pm$ 0.04	56.48
430	440	748	1.0972	90.35 $\pm$ 0.04	56.48
440	450	619	1.0973	90.35 $\pm$ 0.04	56.48
450	460	496	1.0983	90.35 $\pm$ 0.04	56.48
460	470	407	1.1002	90.35 $\pm$ 0.04	56.48
470	480	408	1.0995	90.35 $\pm$ 0.04	56.48
480	490	349	1.0997	90.35 $\pm$ 0.04	56.48
490	500	270	1.1007	90.35 $\pm$ 0.04	56.48
500	510	398	1.0995	90.50 $\pm$ 0.11	110.08
510	520	395	1.1016	90.50 $\pm$ 0.11	110.08
520	530	320	1.1027	90.50 $\pm$ 0.11	110.08
530	540	267	1.1017	90.50 $\pm$ 0.11	110.08
540	550	225	1.1037	90.50 $\pm$ 0.11	110.08
550	560	207	1.1018	90.50 $\pm$ 0.11	110.08
560	570	158	1.1023	90.50 $\pm$ 0.11	110.08
570	580	147	1.1025	90.50 $\pm$ 0.11	110.08
580	590	137	1.1018	90.50 $\pm$ 0.11	110.08
590	600	115	1.1083	90.50 $\pm$ 0.11	110.08
600	610	106	1.1057	90.50 $\pm$ 0.11	110.08
610	620	82	1.1075	90.50 $\pm$ 0.11	110.08
620	630	76	1.1070	90.50 $\pm$ 0.11	110.08
630	640	56	1.1029	90.50 $\pm$ 0.11	110.08
640	650	56	1.1058	90.50 $\pm$ 0.11	110.08
650	660	49	1.1064	90.50 $\pm$ 0.11	110.08
660	670	38	1.1094	90.50 $\pm$ 0.11	110.08
670	680	34	1.1051	90.50 $\pm$ 0.11	110.08
680	690	29	1.1078	90.50 $\pm$ 0.11	110.08
690	700	14	1.1099	90.50 $\pm$ 0.11	110.08
700	710	29	1.1030	90.50 $\pm$ 0.11	110.08
710	720	20	1.1095	90.50 $\pm$ 0.11	110.08
720	730	20	1.1104	90.50 $\pm$ 0.11	110.08
730	740	20	1.1058	90.50 $\pm$ 0.11	110.08
740	750	13	1.1050	90.50 $\pm$ 0.11	110.08
750	770	33	1.1239	90.50 $\pm$ 0.11	110.08
770	800	18	1.1071	90.50 $\pm$ 0.11	110.08
800	850	15	1.1083	90.50 $\pm$ 0.11	110.08
850	1200	17	1.1128	90.50 $\pm$ 0.11	110.08

III. MONTE CARLO SIMULATION

A. Simulation of Inclusive QCD Dijet Mass Spectrum

The inclusive dijet mass spectrum was simulated using the Next–to–leading order (NLO) program JETRAD by Giele, Glover and Kosower [10]. For this analysis the NLO calculations of the dijet mass spectrum used the CTEQ4M [12] parton distribution function (pdf), a renormalisation scale (μ) of $0.5 \times E_T$ where the E_T is the highest E_T parton and a parton clustering algorithm where partons within $1.3\mathcal{R}$ of one another were clustered if they were also within $\mathcal{R} = 0.7$ of their E_T weighted η,ϕ centroid [13]. The E_T of the jets are then smeared using the measured Run 1B jet resolutions [14]. A comparison between the JETRAD calculation and the data with the nominal energy scale correction is shown in Fig 2.

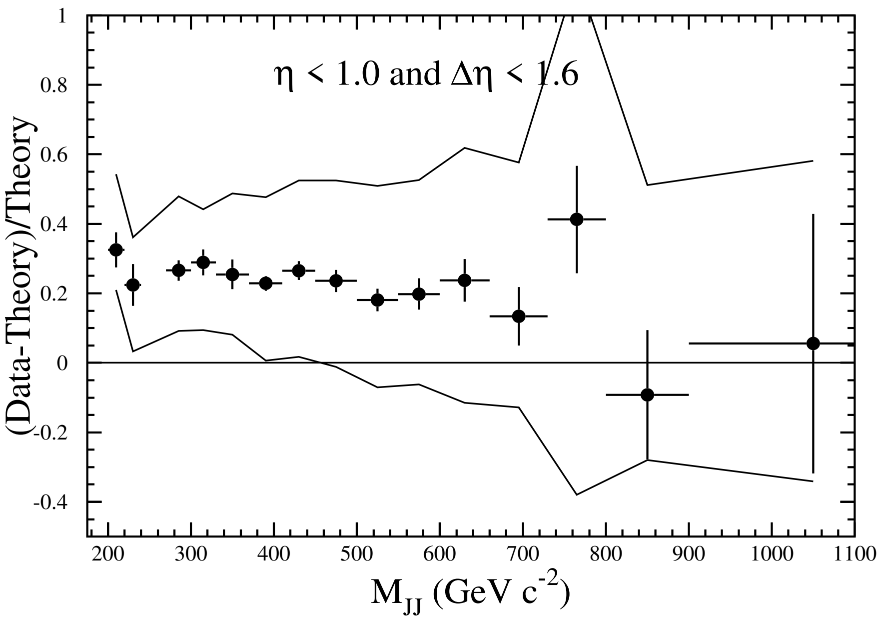

FIG. 2. The difference between the data and the smeared JETRAD NLO QCD prediction normalized to the theoretical prediction ($(\text{Data} - \text{Theory})/\text{Theory}$) using the CTEQ4M pdf and a renormalisation scale $\mu = 0.5 \times E_T$. The upper and lower curves show the effect of the high and low energy scale corrections.

B. Simulation of Signal

Five different models were considered for a possible signal in the dijet mass spectrum. These models were chosen to correspond to five different types of resonance decays. The first model is the decay of an excited quark to a quark and a gluon ($q^* \rightarrow qg$). The second and third models are additional W and Z bosons with the same properties as their standard model counterparts where all possible quark decays are allowed ($W' \rightarrow q\overline{q}'$, $Z' \rightarrow q\overline{q}$). The final models considered are the generic particles X which decays to light quarks ($X \rightarrow q\overline{q}; q = u, d, c, s, b$) and G which decays to gluons ($G \rightarrow gg$).

For each of the models considered a Monte Carlo mass spectrum were generated at 25 GeV intervals from a mass of 200 GeV to 1 TeV. Each of these mass spectrum contains fifty thousand events.

In addition limits were be calculated for the technirho ($\rho_T \rightarrow q\overline{q}, gg$) which will be modelled by a combination of the generic particles X and G.

1. Excited Quark Simulation

The excited quark model used in this analysis is described in Ref [2] with the following model parameters [2]:

$$\begin{aligned} f = f' = f_s &= 1.0 \\ \Lambda^* &= M_{q^*} \end{aligned} \tag{3.1}$$

The excited quark decays, $q^* \rightarrow qg$, were simulated using the PYTHIA event generator with the default settings. The resulting particle jets were smeared with the measured jet resolutions. In Figure 3 the generated line shapes for several excited quark masses are shown. Figure 4 shows the line shape of a 500 GeV q^* with the appropriate statistical errors.

The acceptance (a) of the detector and the applied kinematic cuts for excited quarks is given by the percentage of generated events that pass the cuts (Equation 2.2). The resulting acceptances are given in Table II and figure 5.

The production cross section of excited quarks has been determined at leading order using the PYTHIA generator with the CTEQ3L pdf's [12]. These cross sections are given in Table V.

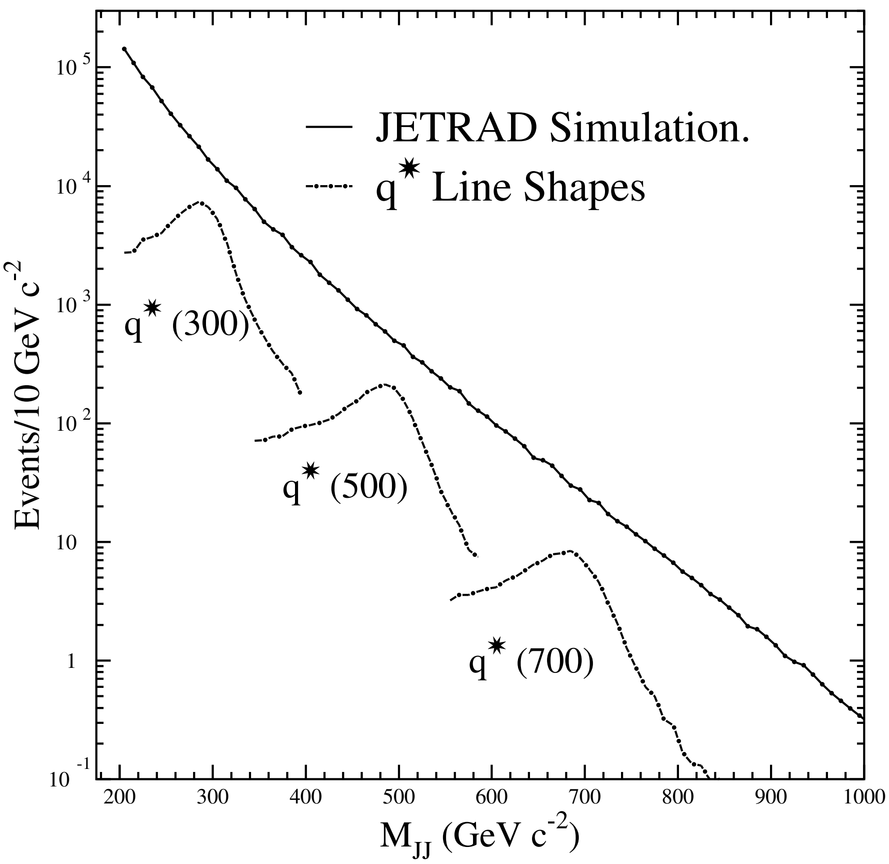

FIG. 3. The JETRAD simulation of the QCD inclusive dijet mass spectrum with the simulated excited quark line shapes for $M_{q^*} = 300$, 500 and 700 GeV. The JETRAD cross section has not been smoothed and the errors produced by the program are shown.

[2] The effect of varying Λ^* on the cross section will be examined when time permits.

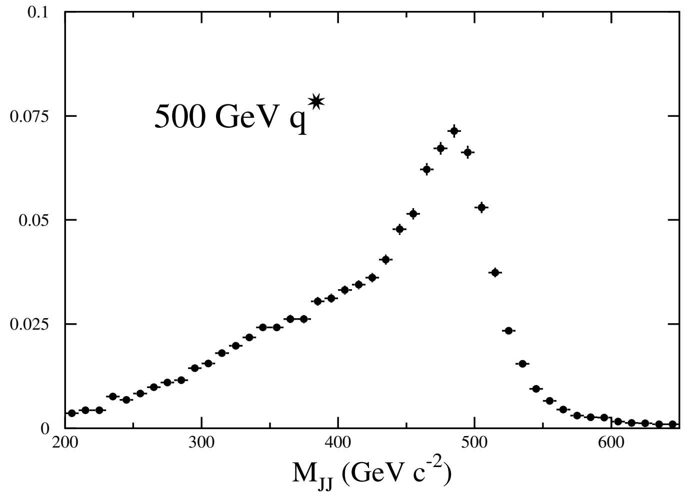

FIG. 4. The line shapes of a 500 GeV q^*. The line shape has been normalized to unit area.

TABLE II. The acceptances for q^*, Z', W', X and G.

Mass (GeV)	q^* (%)	W' (%)	Z' (%)	X (%)	G (%)
200	7.48 ± 0.43	7.54 ± 0.43	7.73 ± 0.43	7.71 ± 0.43	4.44 ± 0.44
225	18.87 ± 0.40	18.29 ± 0.40	17.56 ± 0.41	18.26 ± 0.40	11.61 ± 0.42
250	27.03 ± 0.38	25.20 ± 0.39	23.03 ± 0.39	24.00 ± 0.39	18.23 ± 0.40
275	32.87 ± 0.37	29.98 ± 0.37	25.71 ± 0.38	28.23 ± 0.38	23.17 ± 0.39
300	37.55 ± 0.35	33.56 ± 0.37	28.77 ± 0.38	30.66 ± 0.37	26.85 ± 0.38
325	41.14 ± 0.34	36.48 ± 0.36	31.40 ± 0.37	32.76 ± 0.37	30.58 ± 0.37
350	43.89 ± 0.34	39.04 ± 0.35	34.49 ± 0.36	34.59 ± 0.36	32.85 ± 0.37
375	46.60 ± 0.33	40.26 ± 0.35	36.97 ± 0.35	35.72 ± 0.36	35.58 ± 0.36
400	49.21 ± 0.32	40.92 ± 0.34	39.76 ± 0.35	37.19 ± 0.35	37.11 ± 0.35
425	50.71 ± 0.31	42.70 ± 0.34	41.61 ± 0.34	38.06 ± 0.35	38.46 ± 0.35
450	52.52 ± 0.31	43.55 ± 0.34	43.49 ± 0.34	39.18 ± 0.35	40.32 ± 0.34
475	53.96 ± 0.30	44.57 ± 0.33	44.59 ± 0.33	40.00 ± 0.35	41.15 ± 0.34
500	55.27 ± 0.30	46.03 ± 0.33	45.34 ± 0.33	41.08 ± 0.34	42.53 ± 0.34
525	56.09 ± 0.30	47.03 ± 0.33	46.28 ± 0.33	41.16 ± 0.34	43.81 ± 0.34
550	57.13 ± 0.29	47.38 ± 0.32	46.93 ± 0.33	41.91 ± 0.34	44.12 ± 0.33
575	58.22 ± 0.29	48.08 ± 0.32	47.49 ± 0.32	42.63 ± 0.34	44.87 ± 0.33
600	59.51 ± 0.28	48.02 ± 0.32	47.66 ± 0.32	43.45 ± 0.34	45.72 ± 0.33
625	59.71 ± 0.28	48.86 ± 0.32	48.34 ± 0.32	43.63 ± 0.34	46.04 ± 0.33
650	60.84 ± 0.28	49.58 ± 0.32	48.37 ± 0.32	44.06 ± 0.33	47.11 ± 0.32
675	61.38 ± 0.28	49.70 ± 0.32	48.10 ± 0.32	44.18 ± 0.33	47.39 ± 0.32
700	61.98 ± 0.28	49.55 ± 0.32	48.53 ± 0.32	44.69 ± 0.33	47.58 ± 0.32
725	62.51 ± 0.27	49.74 ± 0.32	47.82 ± 0.32	44.42 ± 0.33	47.92 ± 0.32
750	63.01 ± 0.27	49.42 ± 0.32	47.74 ± 0.32	45.37 ± 0.33	48.60 ± 0.32
775	63.15 ± 0.27	49.74 ± 0.32	47.35 ± 0.32	45.44 ± 0.33	48.58 ± 0.32
800	63.96 ± 0.27	49.13 ± 0.32	46.19 ± 0.33	45.83 ± 0.33	49.06 ± 0.32
825	64.42 ± 0.27	48.40 ± 0.32	45.35 ± 0.33	±	±
850	64.39 ± 0.27	48.04 ± 0.32	44.11 ± 0.33	±	±
875	64.79 ± 0.26	47.26 ± 0.32	42.97 ± 0.34	±	±
900	65.34 ± 0.26	46.08 ± 0.33	41.57 ± 0.34	±	±
925	65.42 ± 0.26	45.59 ± 0.33	39.53 ± 0.35	±	±
950	65.33 ± 0.26	44.10 ± 0.33	38.22 ± 0.35	±	±
975	65.56 ± 0.26	42.52 ± 0.34	36.55 ± 0.36	±	±
1000	65.83 ± 0.26	±	±	±	±

TABLE III. The acceptances for the rapidity cuts ($\eta < 1.0$ and $\Delta\eta < 1.6$) for q^*, Z', W', X and G.

Mass (GeV)	q^* (%)	W' (%)	Z' (%)	X (%)	G (%)
200	36.54 ± 0.36	33.18 ± 0.37	33.22 ± 0.37	31.96 ± 0.37	34.82 ± 0.36
225	38.87 ± 0.35	34.97 ± 0.36	35.38 ± 0.36	33.29 ± 0.37	36.03 ± 0.36
250	41.28 ± 0.34	36.58 ± 0.36	38.15 ± 0.35	33.91 ± 0.36	37.28 ± 0.35
275	43.08 ± 0.34	37.71 ± 0.35	39.98 ± 0.35	35.29 ± 0.36	38.45 ± 0.35
300	44.89 ± 0.33	39.21 ± 0.35	41.92 ± 0.34	35.90 ± 0.36	39.06 ± 0.35
325	46.65 ± 0.33	40.94 ± 0.34	42.92 ± 0.34	36.78 ± 0.36	40.31 ± 0.35
350	47.86 ± 0.32	42.81 ± 0.34	44.15 ± 0.33	37.72 ± 0.35	40.86 ± 0.34
375	49.58 ± 0.32	43.91 ± 0.34	44.99 ± 0.33	38.44 ± 0.35	41.96 ± 0.34
400	51.40 ± 0.31	44.60 ± 0.33	46.17 ± 0.33	39.31 ± 0.35	42.39 ± 0.34
425	52.49 ± 0.31	46.39 ± 0.33	47.02 ± 0.33	39.77 ± 0.35	43.04 ± 0.34
450	53.94 ± 0.30	47.04 ± 0.32	47.84 ± 0.32	40.64 ± 0.34	44.09 ± 0.33
475	54.99 ± 0.30	47.92 ± 0.32	48.28 ± 0.32	41.23 ± 0.34	44.35 ± 0.33
500	56.13 ± 0.30	49.19 ± 0.32	48.77 ± 0.32	42.03 ± 0.34	45.32 ± 0.33
525	56.79 ± 0.29	49.97 ± 0.32	49.41 ± 0.32	42.06 ± 0.34	46.18 ± 0.33
550	57.72 ± 0.29	50.14 ± 0.32	49.84 ± 0.32	42.72 ± 0.34	46.14 ± 0.33
575	58.69 ± 0.29	50.69 ± 0.31	50.27 ± 0.31	43.24 ± 0.34	46.77 ± 0.33
600	59.89 ± 0.28	50.56 ± 0.31	50.50 ± 0.31	43.97 ± 0.34	47.26 ± 0.32
625	60.05 ± 0.28	51.24 ± 0.31	51.03 ± 0.31	44.12 ± 0.33	47.32 ± 0.32
650	61.13 ± 0.28	51.98 ± 0.31	51.16 ± 0.31	44.46 ± 0.33	48.23 ± 0.32
675	61.61 ± 0.28	51.97 ± 0.31	51.08 ± 0.31	44.49 ± 0.33	48.42 ± 0.32
700	62.17 ± 0.28	52.00 ± 0.31	51.47 ± 0.31	45.02 ± 0.33	48.44 ± 0.32
725	62.70 ± 0.27	52.15 ± 0.31	51.05 ± 0.31	44.64 ± 0.33	48.68 ± 0.32
750	63.15 ± 0.27	51.91 ± 0.31	51.06 ± 0.31	45.57 ± 0.33	49.26 ± 0.32
775	63.29 ± 0.27	52.52 ± 0.31	51.05 ± 0.31	45.66 ± 0.33	49.15 ± 0.32
800	64.11 ± 0.27	51.99 ± 0.31	50.42 ± 0.31	45.99 ± 0.33	49.58 ± 0.32
825	64.51 ± 0.27	51.51 ± 0.31	49.91 ± 0.32	±	±
850	64.48 ± 0.27	51.52 ± 0.31	48.99 ± 0.32	±	±
875	64.89 ± 0.26	50.96 ± 0.31	48.57 ± 0.32	±	±
900	65.43 ± 0.26	50.21 ± 0.32	47.67 ± 0.32	±	±
925	65.50 ± 0.26	49.95 ± 0.32	46.43 ± 0.33	±	±
950	65.42 ± 0.26	49.08 ± 0.32	45.75 ± 0.33	±	±
975	65.62 ± 0.26	47.88 ± 0.32	44.51 ± 0.33	±	±
1000	65.88 ± 0.26	±	±	±	±

TABLE IV. The acceptances for the mass cut ($M_{jj} > 200$ GeV) for q^*, Z',W', X and G.

Mass (GeV)	q^* (%)	W' (%)	Z' (%)	X (%)	G (%)
200	20.48 ± 0.66	22.72 ± 0.68	23.27 ± 0.68	24.13 ± 0.69	12.75 ± 0.71
225	48.54 ± 0.51	52.30 ± 0.52	49.64 ± 0.53	54.85 ± 0.52	32.22 ± 0.61
250	65.49 ± 0.41	68.89 ± 0.41	60.35 ± 0.46	70.78 ± 0.41	48.90 ± 0.52
275	76.28 ± 0.33	79.51 ± 0.33	64.31 ± 0.42	79.98 ± 0.34	60.27 ± 0.46
300	83.66 ± 0.27	85.59 ± 0.27	68.63 ± 0.39	85.39 ± 0.28	68.74 ± 0.40
325	88.19 ± 0.22	89.12 ± 0.23	73.16 ± 0.35	89.06 ± 0.24	75.86 ± 0.35
350	91.71 ± 0.19	91.18 ± 0.20	78.12 ± 0.31	91.70 ± 0.21	80.40 ± 0.31
375	94.00 ± 0.16	91.69 ± 0.19	82.18 ± 0.28	92.92 ± 0.19	84.78 ± 0.27
400	95.75 ± 0.13	91.74 ± 0.19	86.12 ± 0.25	94.62 ± 0.17	87.55 ± 0.24
425	96.61 ± 0.11	92.05 ± 0.19	88.50 ± 0.22	95.71 ± 0.15	89.36 ± 0.22
450	97.38 ± 0.10	92.58 ± 0.18	90.90 ± 0.19	96.41 ± 0.13	91.45 ± 0.20
475	98.12 ± 0.08	93.00 ± 0.17	92.35 ± 0.18	97.01 ± 0.12	92.79 ± 0.18
500	98.48 ± 0.07	93.58 ± 0.16	92.95 ± 0.17	97.73 ± 0.10	93.85 ± 0.17
525	98.77 ± 0.07	94.10 ± 0.15	93.67 ± 0.16	97.85 ± 0.10	94.87 ± 0.15
550	98.98 ± 0.06	94.51 ± 0.15	94.16 ± 0.15	98.12 ± 0.09	95.64 ± 0.14
575	99.20 ± 0.05	94.86 ± 0.14	94.48 ± 0.15	98.59 ± 0.08	95.92 ± 0.13
600	99.38 ± 0.05	94.98 ± 0.14	94.37 ± 0.15	98.81 ± 0.07	96.75 ± 0.12
625	99.43 ± 0.04	95.34 ± 0.14	94.71 ± 0.14	98.89 ± 0.07	97.29 ± 0.11
650	99.53 ± 0.04	95.38 ± 0.13	94.54 ± 0.15	99.10 ± 0.06	97.67 ± 0.10
675	99.63 ± 0.04	95.64 ± 0.13	94.16 ± 0.15	99.29 ± 0.06	97.88 ± 0.09
700	99.68 ± 0.03	95.28 ± 0.14	94.28 ± 0.15	99.28 ± 0.06	98.24 ± 0.09
725	99.70 ± 0.03	95.38 ± 0.13	93.67 ± 0.16	99.52 ± 0.05	98.44 ± 0.08
750	99.77 ± 0.03	95.20 ± 0.14	93.49 ± 0.16	99.57 ± 0.04	98.67 ± 0.07
775	99.78 ± 0.03	94.70 ± 0.14	92.74 ± 0.17	99.53 ± 0.05	98.85 ± 0.07
800	99.77 ± 0.03	94.50 ± 0.15	91.61 ± 0.18	99.64 ± 0.04	98.96 ± 0.06
825	99.85 ± 0.02	93.96 ± 0.15	90.87 ± 0.19	±	±
850	99.87 ± 0.02	93.25 ± 0.16	90.05 ± 0.20	±	±
875	99.85 ± 0.02	92.74 ± 0.17	88.48 ± 0.22	±	±
900	99.86 ± 0.02	91.77 ± 0.18	87.21 ± 0.23	±	±
925	99.88 ± 0.02	91.27 ± 0.19	85.15 ± 0.25	±	±
950	99.86 ± 0.02	89.85 ± 0.20	83.54 ± 0.27	±	±
975	99.90 ± 0.02	88.81 ± 0.22	82.12 ± 0.28	±	±
1000	99.92 ± 0.02	±	±	±	±

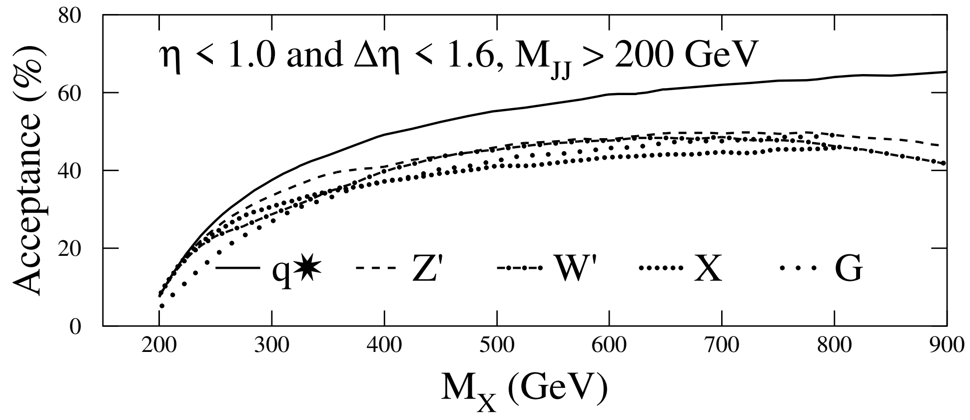

FIG. 5. The acceptances for q^*, Z', W', X and G.

TABLE V. The production cross sections for excited quarks, W' and Z'.

Mass (GeV)	q^* Cross Section $\times$BR (pb)	q^* $\sigma \times$ BR $\times$ a (pb)	Z' Cross Section $\times$BR (pb)	Z' $\sigma \times$ BR $\times$ a (pb)	W' Cross Section $\times$BR (pb)	W' $\sigma \times$ BR $\times$ a (pb)
200	13280.00	993.88	785.57	60.74	386.03	29.10
225	7320.00	1381.14	529.02	92.92	260.44	47.63
250	4229.00	1143.10	366.03	84.29	181.54	45.74
275	2504.00	822.96	258.27	66.41	129.42	38.80
300	1532.00	575.27	186.79	53.73	93.69	31.44
325	952.70	391.98	135.15	42.44	69.45	25.34
350	602.00	264.24	99.12	34.19	51.68	20.18
375	386.20	179.97	73.41	27.14	38.97	15.69
400	251.30	123.67	54.62	21.72	29.80	12.19
425	165.30	83.82	40.79	16.97	22.78	9.73
450	108.60	57.04	30.63	13.32	17.53	7.64
475	72.89	39.33	23.30	10.39	13.57	6.05
500	48.56	26.84	17.56	7.96	10.52	4.84
525	32.69	18.34	13.41	6.21	8.17	3.84
550	22.00	12.57	10.28	4.82	6.36	3.01
575	14.98	8.72	7.80	3.71	4.96	2.39
600	10.22	6.08	6.01	2.86	3.86	1.85
625	6.93	4.14	4.60	2.23	3.03	1.48
650	4.74	2.88	3.53	1.71	2.38	1.18
675	3.21	1.97	2.74	1.32	1.86	0.92
700	2.19	1.36	2.10	1.02	1.45	0.72
725	1.49	0.93	1.62	0.78	1.14	0.56
750	1.01	0.64	1.26	0.60	0.89	0.44
775	0.69	0.44	0.98	0.47	0.70	0.35
800	0.47	0.30	0.77	0.35	0.55	0.27
825	0.31	0.20	0.61	0.28	0.43	0.21
850	0.21	0.14	0.48	0.21	0.34	0.17
875	0.14	0.09	0.38	0.16	0.27	0.13
900	0.10	0.06	0.31	0.13	0.22	0.10
925	0.06	0.04	0.25	0.10	0.17	0.08
950	0.04	0.03	0.21	0.08	0.14	0.06
975	0.03	0.02	0.17	0.06	0.11	0.05
1000	0.02	0.01	0.14		0.09	

2. $\mathbf{W}'$ *and* $\mathbf{Z}'$ *Simulation*

The W' and Z' are modeled using the PYTHIA event generator and the resulting particle jets are smeared using the jet resolutions. Both the W' and Z' are allowed to decay via the quark channels only with $m_t = 175$ GeV (i.e. allowing the decays; $Z' \to d\bar{d}$, $u\bar{u}$, $s\bar{s}$, $c\bar{c}$, $b\bar{b}$, $t\bar{t}$ and $W' \to u\bar{d}$, $c\bar{s}$, $t\bar{b}$ for the appropriate masses).

The acceptances for the W' and Z' are calculated in the same way as for the excited quark. The resulting acceptances are given in table II. The line shapes and acceptances of q^*, W' and Z' are compared in Figures 5 and 6.

The W' and Z' production cross sections are calculated to leading order using the PYTHIA generator using the CTEQ3L pdf's [15] and are then corrected using second order K factors as calculated in Ref. [16]. The resulting cross sections are given in table V.

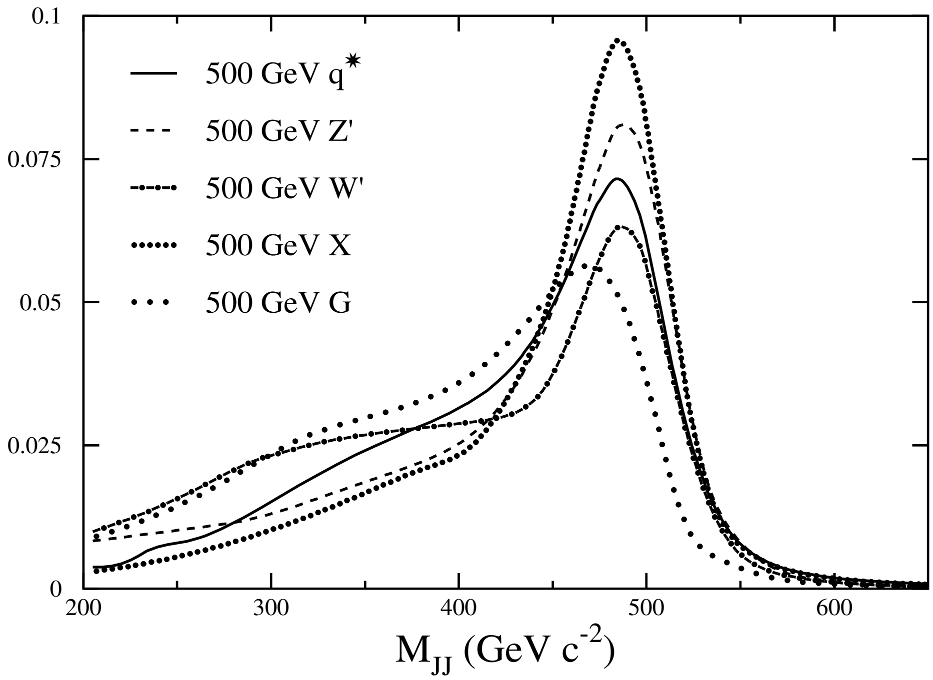

FIG. 6. The line shapes of a 500 GeV q^*, Z', W' X and G . The line shapes have been smoothed and normalized to unit area. The wiggles are due to statistical fluctuations.

3. Simulation of the Generic X *and* G *particles*

The generic particles X and G are generated in PYTHIA using a relativistice Breit–Wigner resonance weighted by parton distribution functions. The width of the resonance will be 2% of the particle mass and the particles will decay isotropically (i.e. the spin equals zero). Both particles will be produced by quark anti–quark annihilation and gluon fusion processes. X decays to the light quarks ($gg, q\bar{q} \to X \to q\bar{q}; q = d, u, s, c, b$) with a branching ratio of 20% to each flavor. G decays to a pair of gluons ($gg, q\bar{q} \to X \to gg$) with a branching ratio of 100% The line shapes for a 500 GeV X and G are shown in Figure 6.

4. Technirho Simulation

Models of walking technicolour [17], which seek to explain weak symetry breaking via the dynamics of a new interaction among techniquarks, predict the existence of colour octet technirhos (ρ_T). We considered a model in which the ρ_T are mass degenerate and only decay to jets ($\rho_T \rightarrow q\overline{q}, gg$).

The cross section for this model is calculated analytically for the rapidity cuts used in this analysis (Table VI) using the CTEQ3L pdf. The line shape and acceptance of the ρ_T was modeled using the line shapes of the generic particles X and G added in the proportion predicted by the relative decay rates (see Figure 7 for an example).

TABLE VI. The cross sections and acceptances for the production of ρ_T (Note that the acceptances are only for the mass cut.).

Mass (GeV)	$\sigma(\rho_T \rightarrow q\overline{q})$ Cross Section (pb)	Acceptance (%)	$\sigma(\rho_T \rightarrow gg)$ Cross Section (pb)	Acceptance (%)	Combined Cross Section $\times$ Acceptance (pb)
200	608.64	24.13 ± 0.69	249.54	12.75 ± 0.71	178.69
225	361.25	54.85 ± 0.52	156.06	32.22 ± 0.61	248.41
250	228.66	70.78 ± 0.41	102.52	48.90 ± 0.52	211.98
275	149.21	79.98 ± 0.34	68.75	60.27 ± 0.46	160.77
300	101.02	85.39 ± 0.28	47.45	68.74 ± 0.40	118.88
325	69.28	89.06 ± 0.24	33.01	75.86 ± 0.35	86.74
350	48.74	91.70 ± 0.21	23.46	80.40 ± 0.31	63.56
375	34.69	92.92 ± 0.19	16.84	84.78 ± 0.27	46.51
400	24.66	94.62 ± 0.17	12.05	87.55 ± 0.24	33.88
425	17.82	95.71 ± 0.15	8.76	89.36 ± 0.22	24.88
450	12.92	96.41 ± 0.13	6.39	91.45 ± 0.20	18.30
475	9.30	97.01 ± 0.12	4.62	92.79 ± 0.18	13.31
500	6.79	97.73 ± 0.10	3.39	93.85 ± 0.17	9.82
525	4.96	97.85 ± 0.10	2.49	94.87 ± 0.15	7.21
550	3.62	98.12 ± 0.09	1.82	95.64 ± 0.14	5.29
575	2.61	98.59 ± 0.08	1.32	95.92 ± 0.13	3.84
600	1.91	98.81 ± 0.07	0.97	96.75 ± 0.12	2.82
625	1.39	98.89 ± 0.07	0.71	97.29 ± 0.11	2.07
650	1.01	99.10 ± 0.06	0.52	97.67 ± 0.10	1.51
675	0.73	99.29 ± 0.06	0.38	97.88 ± 0.09	1.10
700	0.53	99.28 ± 0.06	0.28	98.24 ± 0.09	0.80
725	0.38	99.52 ± 0.05	0.20	98.44 ± 0.08	0.57
750	0.27	99.57 ± 0.04	0.14	98.67 ± 0.07	0.41
775	0.19	99.53 ± 0.05	0.10	98.85 ± 0.07	0.30
800	0.14	99.64 ± 0.04	0.08	98.96 ± 0.06	0.21
825	0.10	±	0.05	±	
850	0.07	±	0.04	±	
875	0.05	±	0.03	±	
900	0.03	±	0.02	±	
925	0.02	±	0.01	±	
950	0.02	±	0.01	±	
975	0.01	±	0.01	±	
1000	0.01	±	0.00	±	

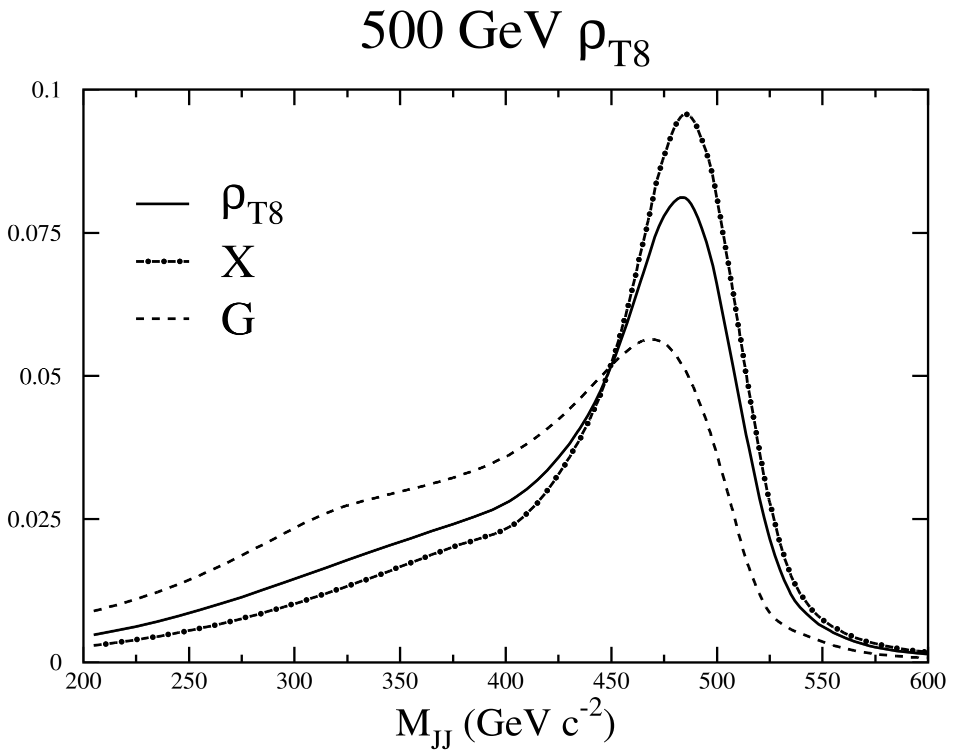

FIG. 7. The line shapes of a 500 GeV ρ_T, X and G . The line shapes have been smoothed and normalized to unit area. The wiggles are due to statistical fluctuations.

IV. DATA FITTING AND THE CALCULATION OF CONFIDENCE LIMITS

The data was fitted using Bayesian techniques (see Ref. [18]). The predicted number of events per bin (μ_i) in the mass spectrum are given by:

$$\mu_i = \left(A\sigma_{QCD_i} + \mathcal{L}N_{X_i}\sigma_X\right) \times \epsilon_{\text{vert}} \times w_i^{-1} \tag{4.1}$$

where σ_{QCD_i} is the predicted JETRAD cross section for the mass bin, A is a normalization factor for the QCD cross section, $\mathcal{L}$ is the integrated luminosity, N_{X_i} is the fraction of the signal in the bin ($\sum N_{X_i} = 1$), σ_X is the signal cross section, ϵ_{vert}, is the efficiency of the vertex cut and w is the event weighting.

The probability that N_i events was observed in a given mass bin is then given by (assuming that N_i follows Poisson statistics):

$$P\left(N_i \mid \sigma_{QCD_i}, \sigma_X, N_{X_i}, A, \mathcal{L}, \epsilon_{\text{vert}}, w_i, I\right) = \frac{e^{-\mu_i}{\mu_i}^{N_i}}{N_i!} \tag{4.2}$$

where I is all other prior information. The probability of observing the set of N_i that makes up the mass spectrum is then given by the product of these probabilities:

$$P\left(N_1, \ldots, N_n \mid \sigma_{QCD_i}, \sigma_X, N_{X_i}, A, \mathcal{L}, \epsilon_{\text{vert}}, w_i, I; (i = 1 \ldots n)\right) = \prod_{i=1}^{n} \left(\frac{e^{-\mu_i}{\mu_i}^{N_i}}{N_i!}\right) \tag{4.3}$$

We are interested in determining the probability distribution for σ_X, so we need to apply Bayes' theorem:

$$P\left(\sigma_X \mid N_i, \sigma_{QCD_i}, N_{X_i}, A, \mathcal{L}, w_i, I; (i = 1 \ldots n)\right) =$$
$$\frac{\int_{(\sigma_{QCD_i}, X_i, A, \mathcal{L}, w_i)} P\left(N_1, \ldots, N_n \mid \sigma_{QCD_i}, \sigma_X, N_{X_i}, A, \mathcal{L}, \epsilon_{\text{vert}}, w_i, I; (i=1\ldots n)\right)}{\int_{(\sigma_X, \sigma_{QCD_i}, X_i, A, \mathcal{L}, w_i)} P\left(N_1, \ldots, N_n \mid \sigma_{QCD_i}, \sigma_X, N_{X_i}, A, \mathcal{L}, \epsilon_{\text{vert}}, w_i, I; (i=1\ldots n)\right)} \tag{4.4}$$

When solving this equation we make the following assumptions about the prior probability distributions: σ_X and A have flat priors; σ_{QCD_i}, $\epsilon_{\rm vert}$, $\mathcal{L}$ and w_i all have Gaussian priors; N_{X_i} has a Poisson prior. The integral equation will be solved using standard numerical integration techniques.

The uncertainty in $\mathcal{L}$ is 8% , and the uncertainty in the event weights is 1% . The uncertainties in the JETRAD QCD spectrum [3] are as given by the program and the signal line shapes uncertainties are determined by the size of the sample. All other errors are given in table I.

The uncertainty in the energy scale was incorporated into the method by using eleven different mass spectra, each one corresponding to a different energy scale correction. The eleven energy scale corrections were the nominal correction and $\pm 0.2\sigma$, $\pm 0.4\sigma$, $\pm 0.6\sigma$, $\pm 0.8\sigma$ and $\pm 1.0\sigma$, where $\pm\sigma$ are the difference between the nominal and high and low energy corrections respectively. The eleven different energy corrections are applied on an event by event basis to generate the corresponding mass spectra. The probability distributions were calculated separately for each of these mass spectra and combined to form the final probability distribution.

A. Fitting the Data with the Inclusive QCD Dijet Mass Spectrum

The data were fitted to QCD NLO prediction by using the above method with σ_X set equal to zero. The resulting probability distribution is depicted in Fig 8 as a function of the normalization A. This plot shows that the JETRAD prediction best matches the data with an energy scale correction of $+0.4\sigma$ with a normalization of $A = 1.33$. A comparison of the JETRAD and the data is given in Fig 9. The χ^2 of the comparison is 11.03 for 15 degrees of freedom.

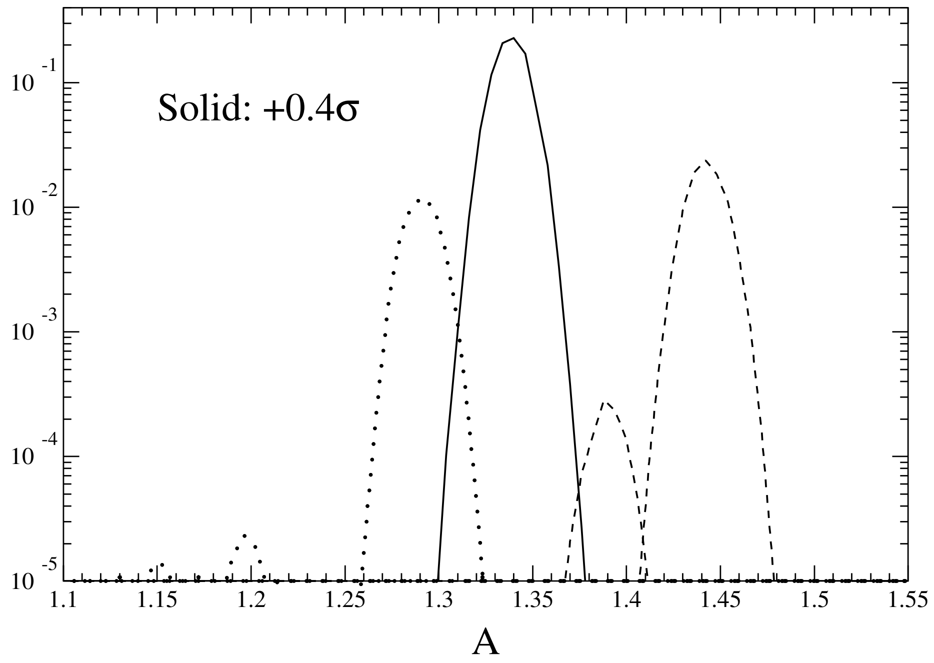

FIG. 8. The probability distribution for a fit to the data using the JETRAD QCD prediction. The solid line shows the probability distribution for an energy correction of $+0.4\sigma$.

[3] These errors may be too small by design. I will be looking into making an improved estimate.

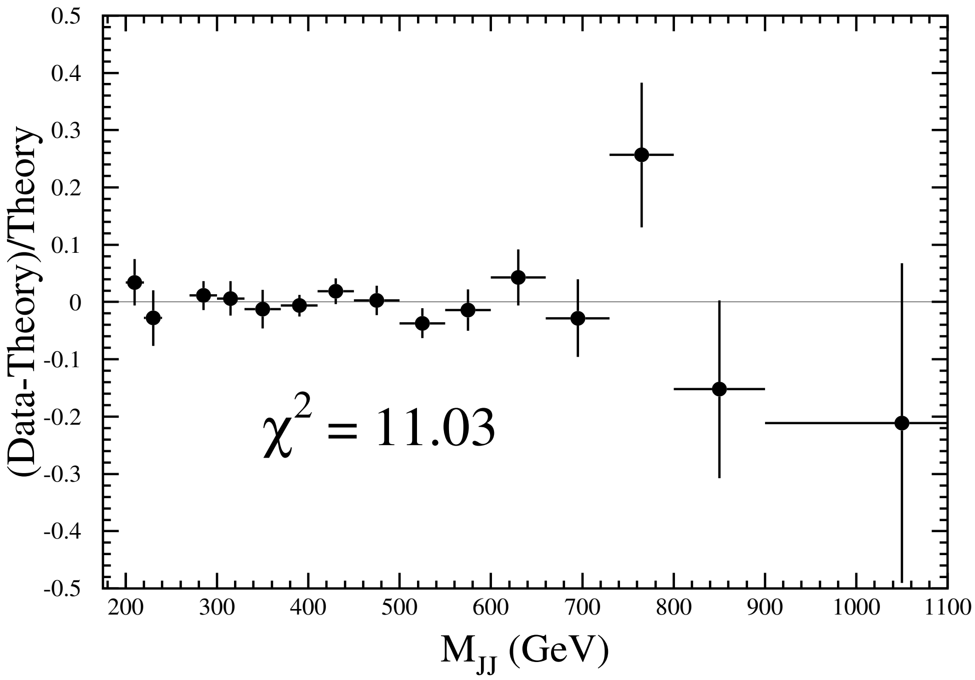

FIG. 9. The difference between the data with an energy scale correction of $+0.4\sigma$ and the smeared JETRAD NLO QCD prediction normalized to the theoretical prediction ((Data − Theory)/Theory) using the CTEQ4M pdf and a renormalization scale $\mu = 0.5 \times E_T$.

B. Extraction of Signal Limits

The 95% Confidence Limits on the production cross section for the four theoretical models were extracted. This is done by determining the value of σ_X that 95% of the probability distribution lies below (for example see Fig 10). Due to the amount of time it takes to run the numerical integrations the value of A has been restricted to: $1.28 < A < 1.40$.

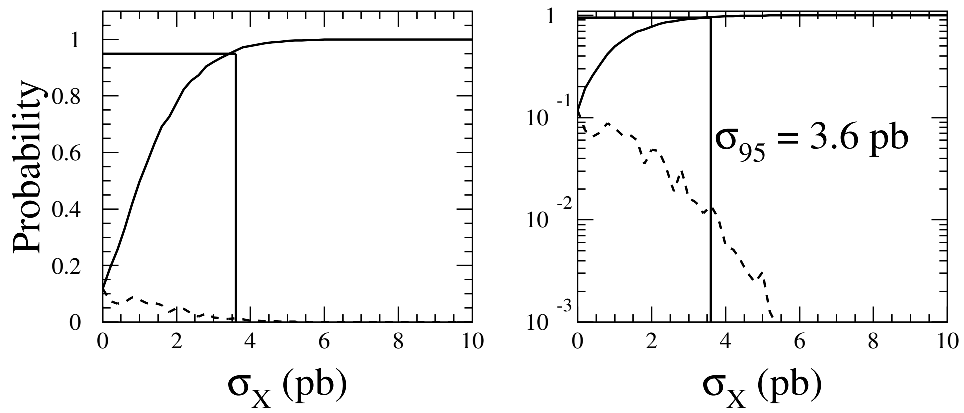

FIG. 10. The probability distribution for an excited quark of mass 500 GeV as a function of σ_X. The dashed line shows the probability distribution as a function of σ_X and the solid line shows the sum of the probability distribution. The 95% upper confidence limit on the production cross section is 3.6 pb. The wiggles in the probaility distribution function are due too statistical fluctuations in the numerical integration.

The cross section limits for the q^*, W', Z', X, G, and ρ_T are given in table VII and are depicted in Fig 11.

The q^* cross section limits is compared to the predicted cross section in Fig 12. We exclude excited quarks with $M_{q^*} < 725$ GeV. The W' cross section limits are compared with predicted cross section in Fig 13. The W' is ruled out for $340 < M_{W'} < 680$ GeV and the Z' (Fig 14) is ruled out for $365 < M_{Z'} < 615$ GeV. Finally limits on ρ_T production are given in Fig 15 and the ρ_T is ruled out for $230 < M_{\rho_T} < 700$ GeV.

TABLE VII. The 95% CL on the production cross section ($\sigma_X \times$ BR $\times$ a) for the q^*, Z', W', H0$'$and ρ_T models.

Mass (GeV)	q^* (pb)	W' (pb)	Z' (pb)	X (pb)	G (pb)	ρ_T (pb)
200	110.00	295.00	205.00	265.00	205.00	265.00
225	195.00	315.00	315.00	255.00	300.00	270.00
250	140.00	195.00	200.00	180.00	185.00	190.00
275	110.00	90.00	95.00	90.00	155.00	100.00
300	64.00	66.00	64.00	62.00	86.00	70.00
325	52.00	52.00	46.00	48.00	64.00	52.00
350	29.00	29.00	25.00	27.00	47.00	31.00
375	15.00	13.00	12.00	12.00	22.00	14.00
400	9.50	10.00	8.00	7.50	13.50	8.50
425	8.00	9.00	7.00	6.50	10.00	7.00
450	6.80	7.60	5.80	5.50	8.50	6.50
475	5.00	5.40	4.60	4.00	7.00	5.00
500	3.40	3.80	3.00	2.50	5.00	3.50
525	2.40	2.80	2.00	2.00	3.50	2.50
550	1.90	2.20	1.70	1.50	2.50	1.50
575	1.70	2.00	1.50	1.00	2.00	1.50
600	1.75	2.05	1.60	1.40	2.00	1.60
625	1.65	1.90	1.60	1.30	2.00	1.50
650	1.40	1.65	1.30	1.10	1.80	1.30
675	1.10	1.25	1.05	0.90	1.50	1.00
700	0.99	1.14	0.87	0.70	1.20	0.80
725	0.96	1.17	0.96	0.70	1.10	0.80
750	1.05	1.29	1.08	0.80	1.20	1.00
775	0.93	1.17	0.93	0.70		0.90
800	0.69	0.84	0.66			
825	0.48		0.42			
850	0.36		0.36			
875	0.33		0.36			
900	0.33					
925	0.30					
950	0.27					
975	0.27					
1000						

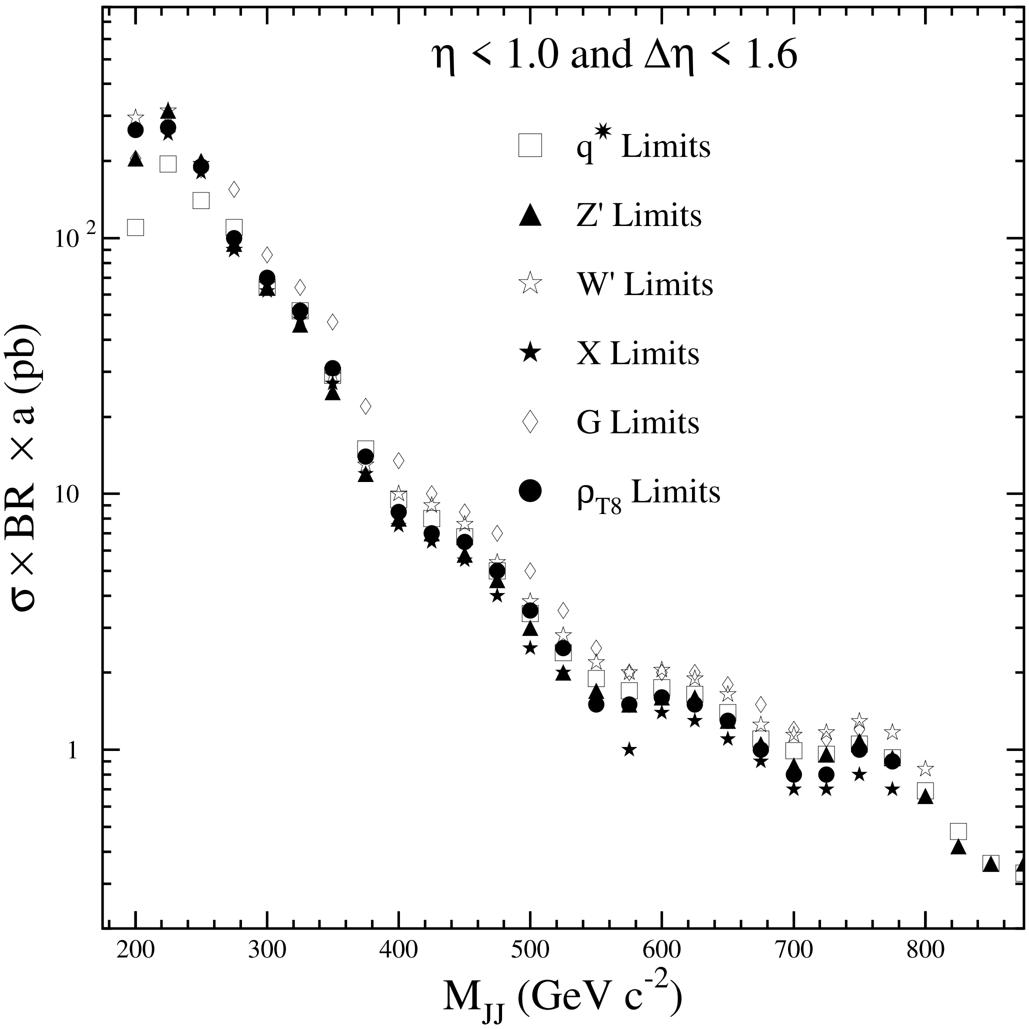

FIG. 11. The 95% CL on the production cross section (σ_X × BR × a) for the q^*, Z', W', X, G and ρ_T models.

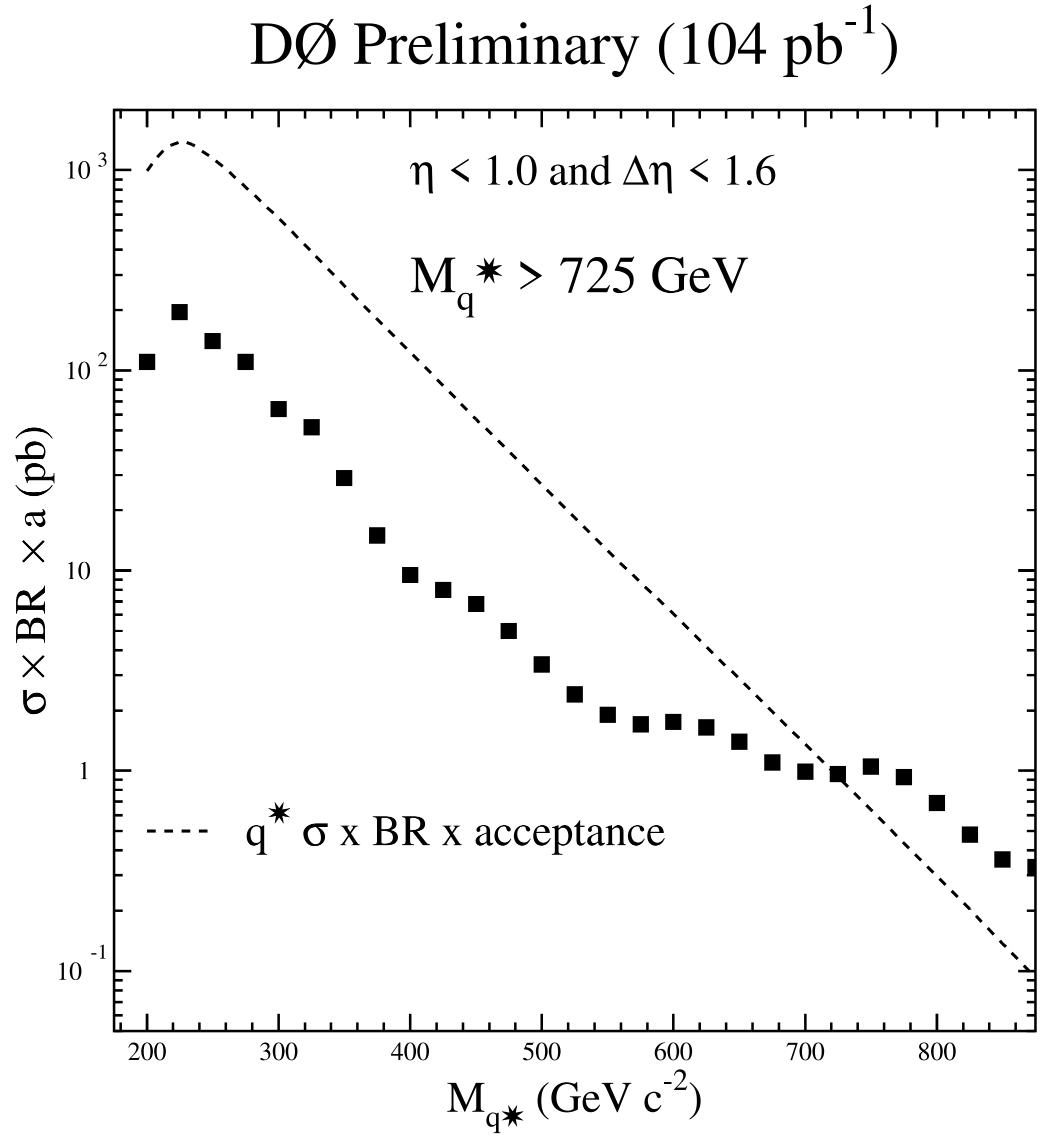

FIG. 12. The 95% CL on the production cross section ($\sigma_X \times \mathrm{BR} \times a$) for the q^* (solid squares) compared with the predicted cross section (dashed line). Values of $M_{q^*} < 725$ GeV are excluded at the 95% CL.

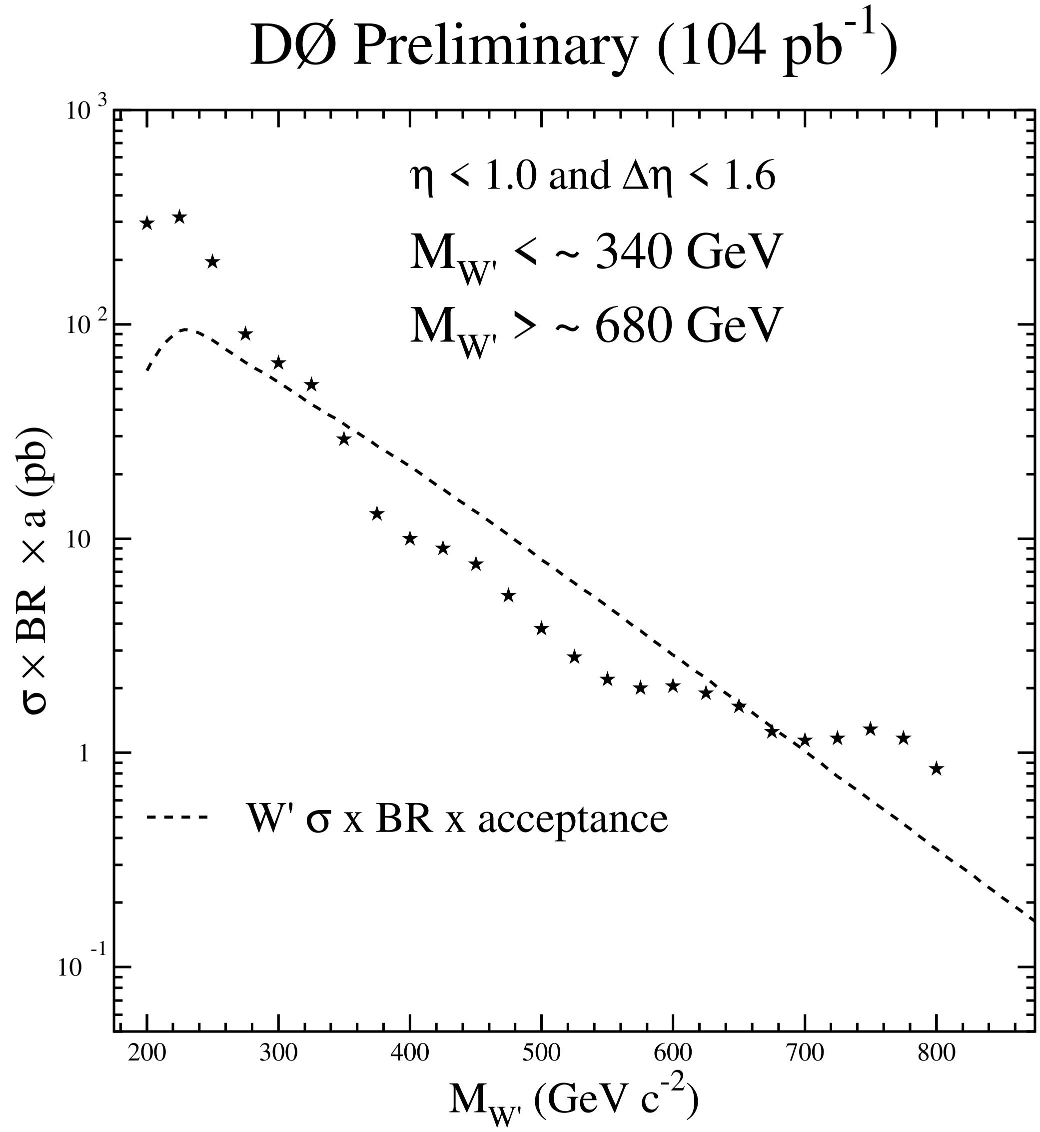

FIG. 13. The 95% CL on the production cross section ($\sigma_X \times$ BR $\times$ a) for the W' (solid stars) compared with the predicted cross section (dashed line). Values of $340 < M_{W'} < 680$ GeV are excluded at the 95% CL.

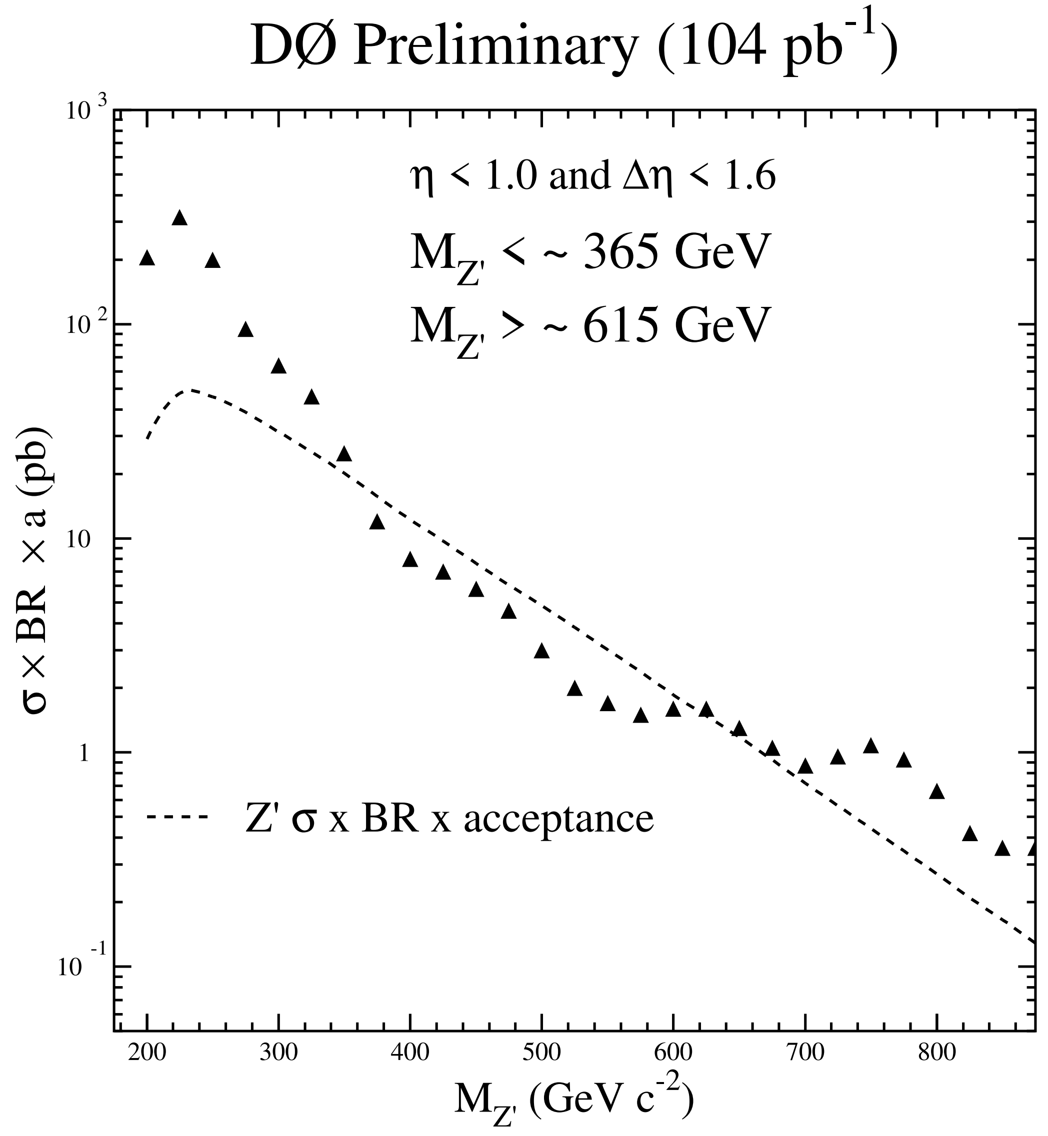

FIG. 14. The 95% CL on the production cross section ($\sigma_X \times \mathrm{BR} \times a$) for the Z' (solid triangles) compared with the predicted cross section (hashed line). Values of $365 < M_{Z'} < 615$ GeV are excluded at the 95% CL.

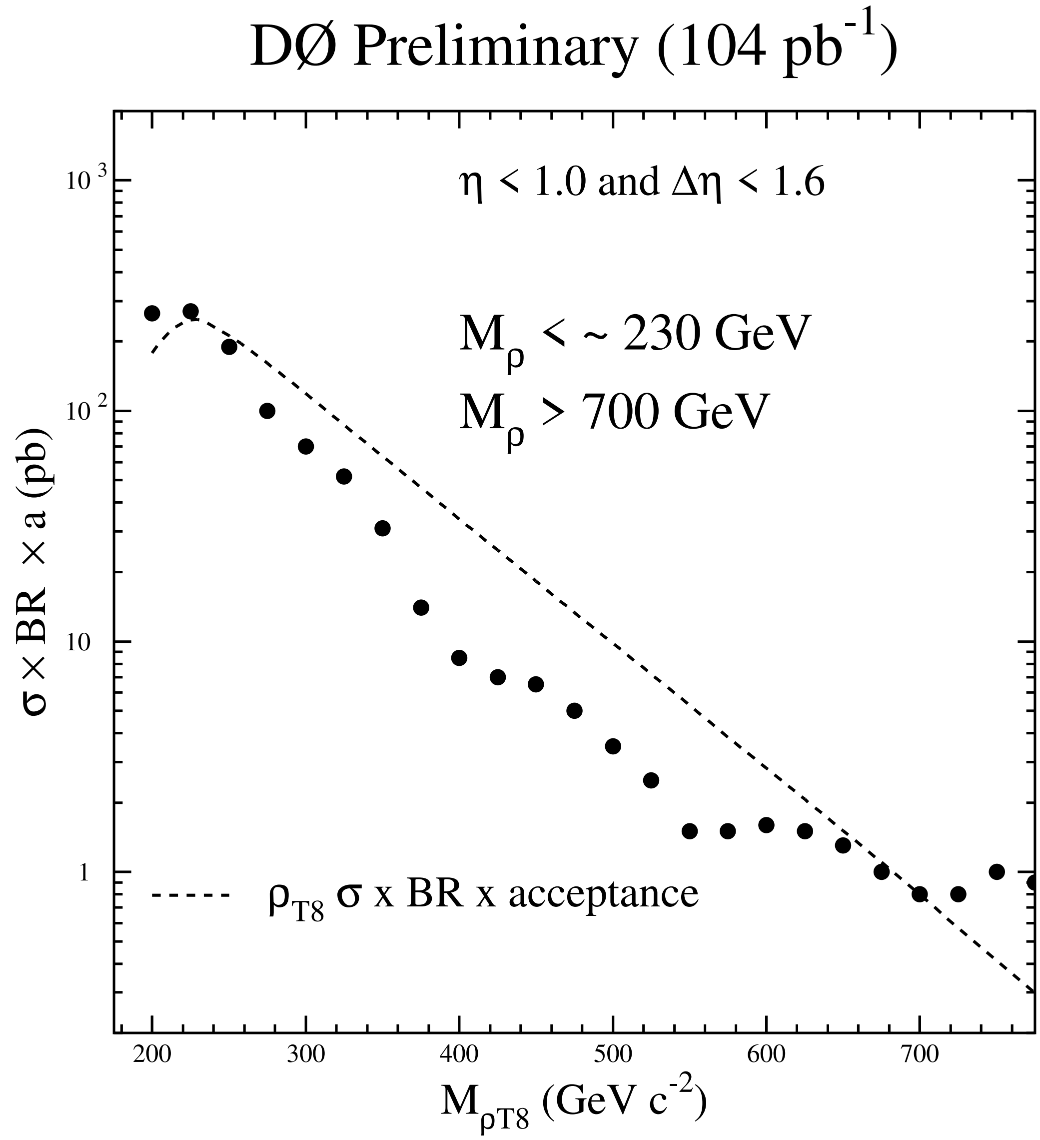

FIG. 15. The 95% CL on the production cross section (σ_X × BR × a) for the ρ_T (solid circles) compared with the predicted cross section (dashed line). Values of XXX $< M_{\rho T} <$ XXX GeV are excluded.

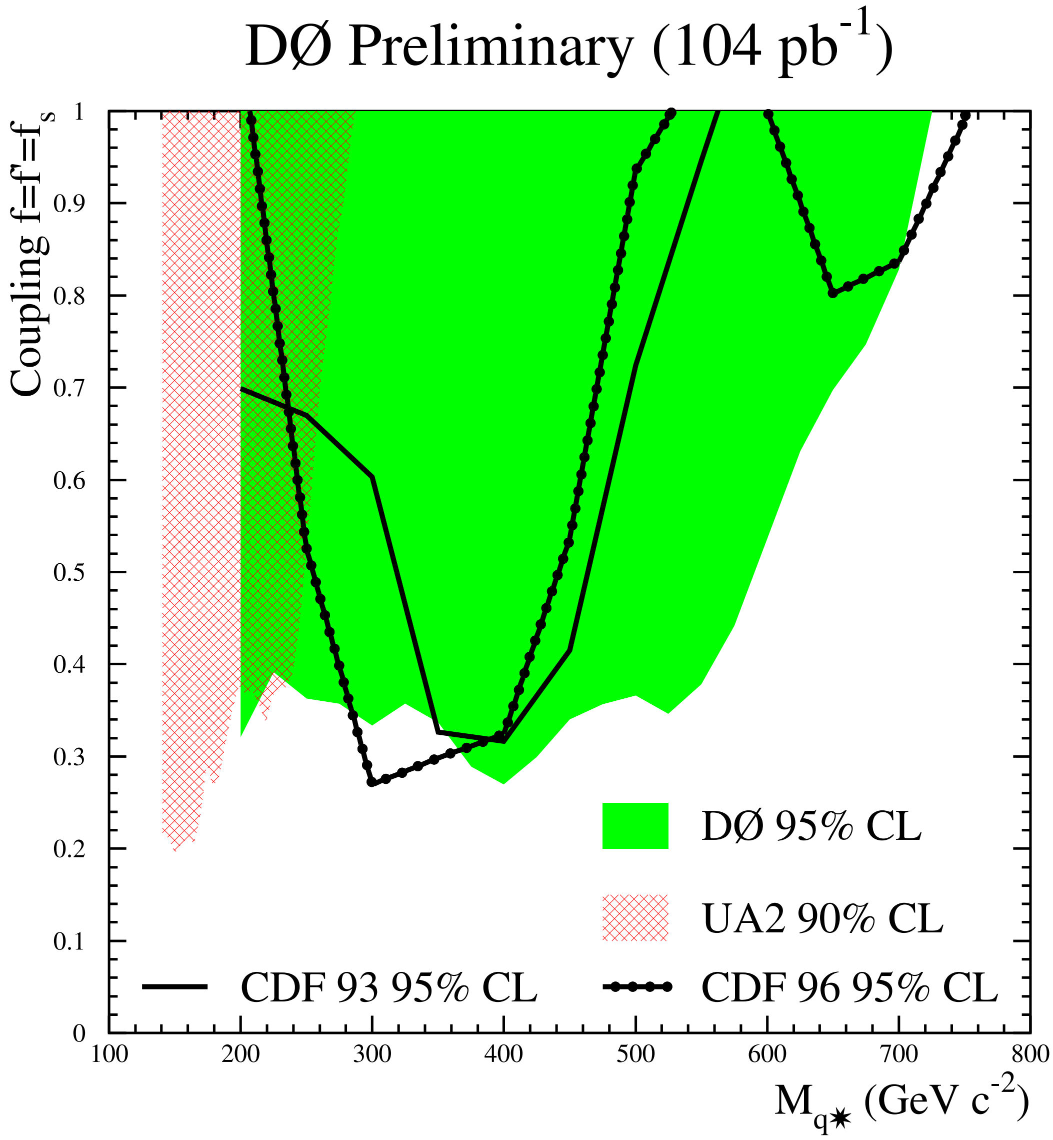

FIG. 16. A comparsion of the DØ 95% CL on the production cross section ($\sigma_X \times$ BR $\times$ a) for the q^* in terms of the excited quark coupling parameters (Equation 3.1) to those limits measured by UA2 [5] and CDF [6,19] (The CDF 93 (solid) curve shows the results published in PRL and the CDF 96 (solid with dots) curve the limits presented at DPF 96).

V. CONCLUSION

A search for new particles decaying to dijets at the DØ detector has been carried out. Preliminary 95% Confidence limits on the cross section of excited quarks, W', Z', X, G and ρ_T have been measured.

In conclusion we see no evidence for new particle production and set preliminary 95% confidence limits on several models of new particle production.

[1] P. Bagnaia and S. D. Ellis, **Ann. Rev. Nucl. Part. Sc. 38**(1988) 659.
T. Akesson *et al.*, Phys. Lett. **B118**, 82 (19;)
M. Banner *et al.* (UA2 Collaboration), Phys. Lett. **B118**, 203 (1982)

[2] U. Baur, M. Spira and P.M. Zerwas, *Excited–quark and –lepton production at hadron colliders*, Phys. Rev. **D42**, 815 (1990)

[3] P. Frampton and S. Glashow, Phys. Lett. **B190**, 157 (1987);
J. Bagger, C. Schmidt and S. King, Phys. Rev. **D42**, 815 (1990)

[4] J. Alitti et al. (UA2 Collaboration), Zeit. Phys. **C49**, 17 (1991)

[5] J. Alitti et al. (UA2 Collaboration), Nucl. Phys. **B400**, 3 (1993)

[6] F. Abe et al. (CDF Collaboration), Phys. Rev. Lett. **74**, 3538 (1995)

[7] I.A. Bertram and S. Choi, "The Dijet Mass Spectrum at DØ", DØ Internal Note 2864.

[8] B. Blazey and B. Hirosky, "Comparison of Central Large E_T Jet Production with QCD Expectations", DØ Internal Note ???? (Run IB Analysis)

[9] M. Bhattacharjee et al., "Efficiencies of the Standard Jet Cuts for cone sizes: 0.3, 0.5, 0.7", DØ Internal note 2197.
V. Elvira *et al.*, "A Study of Standard Jet Cuts and their Efficiencies Using DØ Collider Data", DØ Internal note 1763.

[10] W.T. Giele, E.W.N. Glover and D.A. Kosower, "The Two–Jet Differential Cross Section with $\mathcal{O}(\alpha_s^3)$ in Hadron Collisions", Phys. Rev. Lett. **73**, 2019 (1994)

[11] H.U. Bengtsson and T. Sjöstrand, Computer Physics Commun. **46** (1987) 43.

[12] CTEQ Collaboration, J. Botts, *et al.*, Phys. Lett. **B304**, 159 (1993)

[13] B. Abbott et al, "Fixed Cone Jet Definition in DØ and R_{sep}", DØ Internal Note 2885

[14] M. Bhattacharjee et al., "Jet Energy Resolutions", DØ Internal note 2887

[15] A.D. Martin, R.G. Roberts, and W.J. Stirling, Phys. Lett. **B306**, 145 (1993) and erratum Phys. Lett. **B309**, 492 (1993)

[16] R. Hamberg, W.L. van Neerven and T. Matsuura, Nucl. Phys. **B359**, 343 (1991)

[17] K. Lane and M. Ramana, Phys. Rev. **D44**, 2678 (1991);
E. Eichten and K. Lane, Phys. Lett. **B327**, 129 (1994).

[18] I. Bertram et al., "A Recipe for the Construction of Confidence Limits", DØ Internal Note 2775A (Dec 1995).

[19] A. Goshaw (for the CDF Collaboration), Di–jet Production frojm $\overline{p}p$ Collisions at 1.8 TeV", Presented at the 1996 A.P.S. Division of Particles and Fields Meeting, Minneapolis, Minnesota, August 10–15, 1996.

APPENDIX A: THE EFFECT OF THE PRODUCTION PROCESS ON THE DECAY LINE SHAPE OF A PARTICLE X

The effect of the production process on the decay line shape of the process $X \to$ jets were studied by examining a toy Monte Carlo based on a Breit–Wigner resonance:

$$\hat{\sigma}_X(\hat{s}) = \frac{\hat{s}}{M^2} \frac{\Gamma_i \Gamma_{\text{tot}}}{\left(\left(\hat{s} - M^2\right)^2 + \left(\frac{\hat{s}\Gamma_{\text{tot}}}{M}\right)^2 \right)} \tag{A1}$$

where $\hat{s} = x_1 x_2$ 1800 GeV, M is the resonance mass (500 GeV), Γ_{tot} is the resonance width (50 GeV) and Γ_i is the width of the production process (12.5 GeV). Values of x_1 and x_2 were then generated with a uniform distribution over the range $0.1 < x < 0.8$. Only events with $0.1 < x_1 x_2 < 0.8$ and that pass the kinematic cuts of the analysis (applied by allowing X to decay isotropically, see Equation 2.2 for details of the cuts) were allowed to contribute to the cross section. The resulting resonance is plotted in Fig 17.

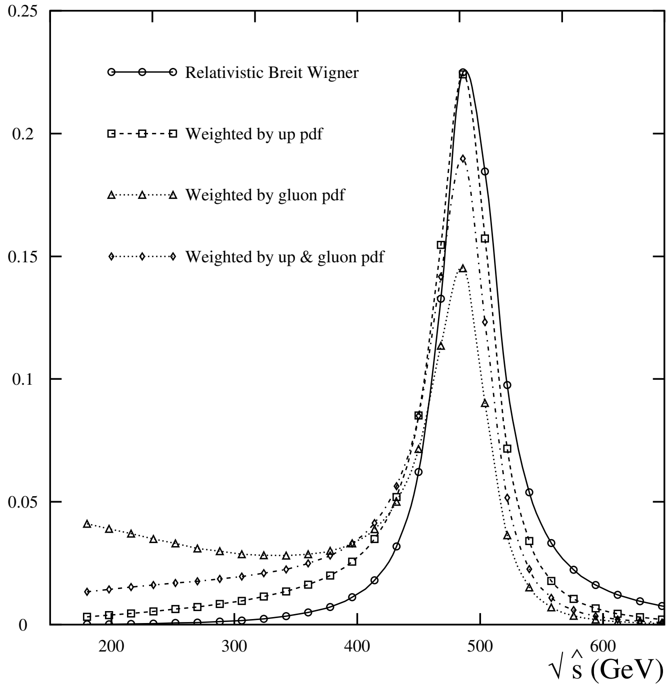

FIG. 17. The relativistic Breit–Wigner resonance produced by the Monte Carlo integration normalised to an area of 1. The dashed and dotted lines give the corresponding resonance shapes for the Breit–Wigner weighted by the various parton distribution functions.

The effect of the parton distribution functions on the line shapes was evaluated by weighting Equation A1 by the appropriate pdf and integrating over the possible values of x_1 and x_2:

$$\sigma_X(\hat{s}) = \int dx_1 \int dx_2 \hat{\sigma}_X(\hat{s}) x_1 f_1\left(x_1, Q^2\right) x_2 f_2\left(x_2, Q^2\right) \tag{A2}$$

where Q^2 is given by $\hat{s}$. This is evaluated using the CTEQ3L pdf for three different production models. The first is $q\bar{q} \to X$ which uses the “up” pdf for f_1 and f_2, the second process is $qg \to X$ which uses the “up” and “gluon” pdf’s and the last process is $gg \to X$ which uses the “gluon” distributions. The resulting line shapes are given in Fig 17. These line shapes show that the decay line shape of a particle X is significantly effected by the parton distribution function via the production process. This is due to the vastly different shapes of valence quark distributions and the sea quark and gluon distributions.

The effect of varying the pdf used has been examined by looking at the various CTEQ4 pdf’s and comparing the resulting line shapes. The pdf's used were CTEQ4L which is the standard LO pdf, CTEQ4M the standard NLO pdf, CTEQ4D the DIS[4] NLO pdf, CTEQ4HJ which has had the gluon distribution adjusted to fit the mythical CDF inclusive jet excess at high E_T and CTEQ4LQ which uses data at lower Q values in its fit. The results of using these pdf's with Equation A2 is given in Fig 18. This shows that if the production mechanism of particle X is dominated by gluon fusion then the decay line shape will be heavily dependent on the gluon pdf. This variation does not effect processes that are generated by quark annihilation as the valance distributions have much smaller uncertainties.

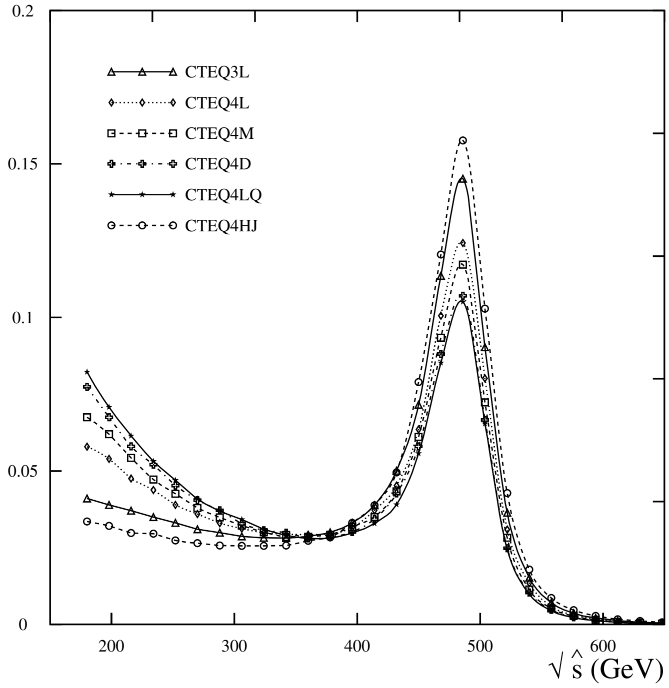

FIG. 18. The relativistic Breit–Wigner resonance produced by the Monte Carlo integration convoluted with various gluon parton distribution functions and normalised to an area of 1.

The effect of the width ($\Gamma_{\rm tot}$) on the distribution was estimated by varying $\Gamma_{\rm tot}$ from $0.10M$ to $0.01M$. The results of this are shown in Fig 19. As the width decreases the effect of the pdf's are minimized. When we are looking at resonances with a negligible width (eg. 1%) then we can ignore the production mechanism of resonance (the effects of the different pdf's are also negligible).

---

[4] An alternative to the $\overline{\rm MS}$ QCD resummation scheme

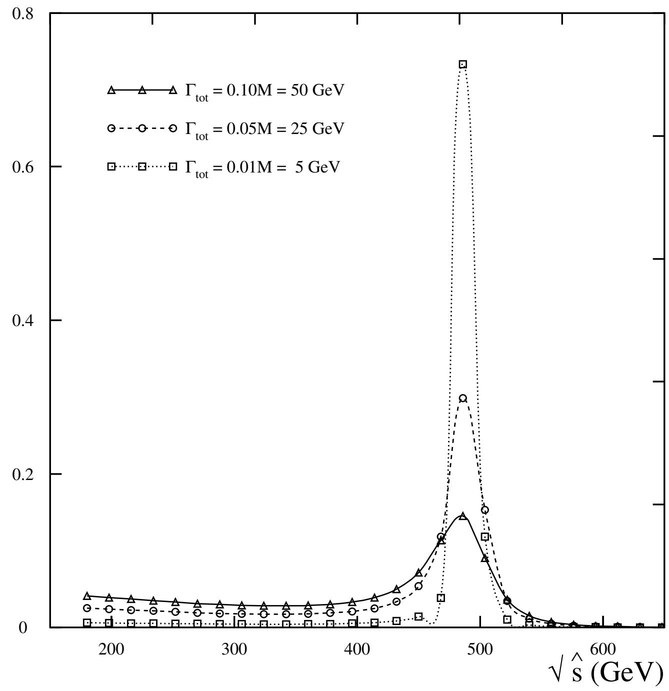

FIG. 19. The relativistic Breit–Wigner resonance produced by the Monte Carlo integration convoluted with the CTEQ3L pdf with $\Gamma_{\rm tot} = 0.10M, 0.05M, 0.01M$ and normalised to an area of 1.

APPENDIX B: THE EFFECT OF THE DECAY PRODUCTS ON THE DECAY LINE SHAPE.

The effect of the decay products on the decay line shape was examined using the generic particles X and G generated by PYTHIA at 500 GeV. Each process has been generated with fifty thousand events and smeared by the DØ jet resolutions, the results are given in Fig 20. This plot clearly shows that when a particle decays to gluons the line shape is broadened significantly. Hence it is important to use an appropriate line shape when determining limits for particles decaying to two–jets.

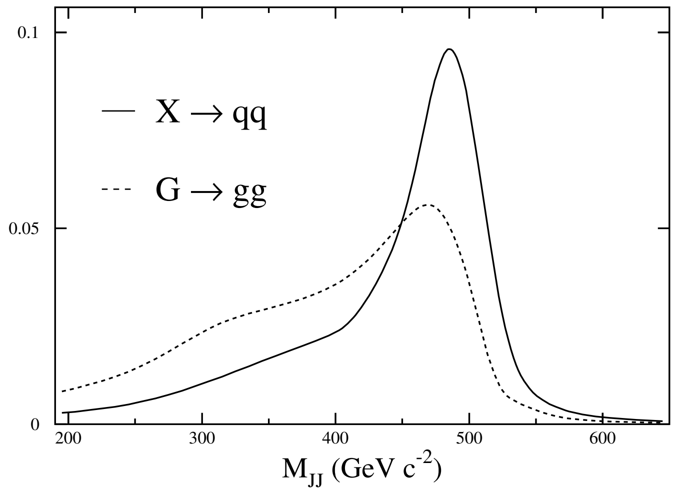

FIG. 20. The line shapes of a 500 GeV X and G (the curves have been smoothed and normalized to unit area).

APPENDIX C: TEST OF BAYSIAN FITTING TECHNIQUE

The fitting technique will be tested by applying the method described in Section IV to a set of simulated dijet mass spectra.

The simulated spectra are generated from the JETRAD simulation of the inclusive QCD dijet mass spectrum (section III A). The mean number of events per ten GeV mass bin is given by the predicted cross section for that bin times the integrated luminosity for the bin. Ten random spectra are then produced by smearing the predicted number of events per bin by poisson statistics.

The resulting spectra are then fitted with the JETRAD simulation and the excited quark line shapes of various masses. The resulting 95% CL on the production cross section of excited quarks is compared with those obtained from fitting the data (Figure 21).

This test shows that the limits obtained in this analysis are consistent with the limits predicted by the size of the data sample.

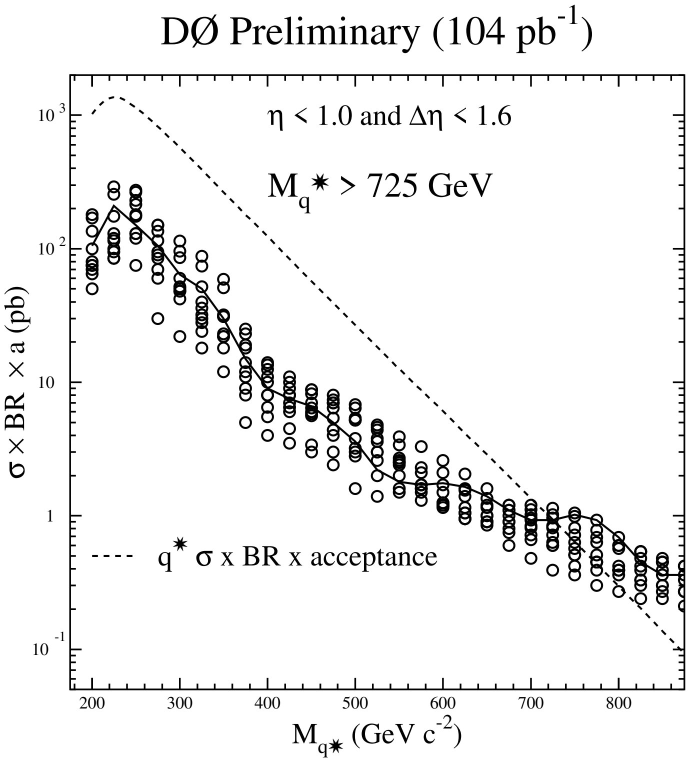

FIG. 21. The 95% CL on the production cross section ($\sigma_X \times \mathrm{BR} \times a$) for the q^* (solid line) compared with the predicted cross section (dashed line). The open circles show the 95% CL obtaned from fitting the ten simulated dijet mass spectra.

APPENDIX D: INHERENT BIASES IN THE ANSATZ FUNCTION METHOD

Previous searches for particles decaying to dijets [4–6] have used a method where the QCD inclusive dijet mass spectrum is fitted by an ansatz function plus a signal line shape to determine limits on the production cross section for various theoretical particles.

The reliability of this method depends on how well the ansatz function represents the QCD inclusive dijet mass spectrum.

To test this, one hundred dijet mass spectra were generated from the JETRAD simulation (see previous section) and fitted with an ansatz function and an excited quark line shape. The ansatz function used in this analysis is:

$$F_i = \int_{X_{\mathrm{min}}}^{X_{\mathrm{max}}} A \left(\frac{M}{100}\right)^{-\alpha} \left(1 - \frac{M}{1800}\right)^{-\beta} dM \tag{D1}$$

where A gives the normalization and α and β are fit parameters.

For each of the one hundred spectra fitted the signal size N_X and its error ΔN_X will be determined. The average of N_X and ΔN_X will then be used to determine the 95% CL on the excited quark production cross section. This is done by assuming that the probability density function is a Gaussian with a mean given by $\overline{N_X}$ and width $\overline{\Delta N_X}$, the 95% CL on the cross section ($\sigma_{95\%}$) is then given by the value of the cross section such that 95% of the physical part of the probability density function is below this value.

Since the spectra being fitted are derived from a NLO QCD calculation the value of $\overline{N_X}$ should be zero. Any deviation from zero is the result of an inherent bias in the ansatz method. Figure 22 shows that there are systematic biases in the value of $\overline{N_X}$.

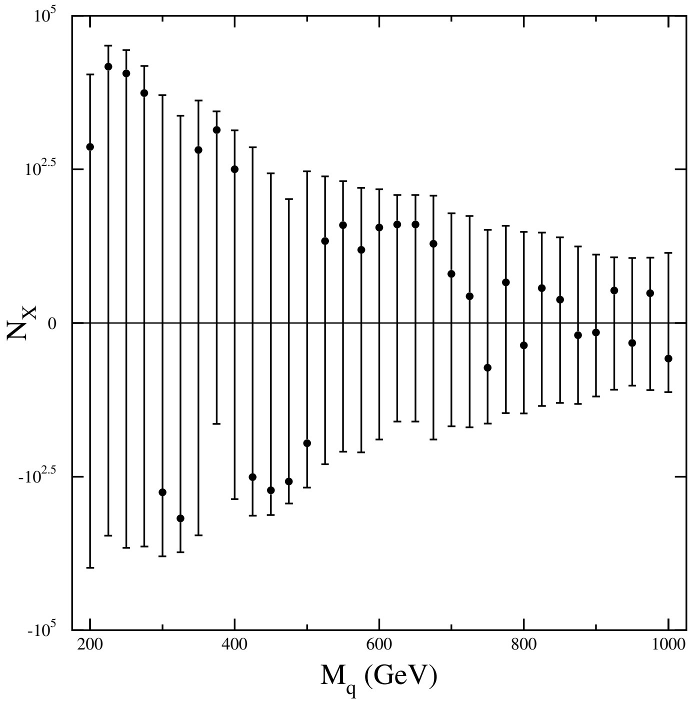

FIG. 22. The values of $\overline{N_X}$ (solid circles) and $\overline{\Delta N_X}$ (error bars) obtained from fitting the simulated dijet mass spectra.

If there was no bias in the ansatz fitting method the 95% CL on the production cross section would be given by $1.96 \times \overline{\Delta N_X}$. A measure of the bias in the ansatz is the the difference between $\sigma_{95\%}$ and $1.96 \times \overline{\Delta N_X}$:

$$\text{Bias} = \frac{\sigma_{95\%} - (1.96 \times \overline{\Delta N_X})}{1.96 \times \overline{\Delta N_X}} \tag{D2}$$

The resulting biases are depicted in Figure 23. The plot clearly shows that the resulting 95% CL on the production cross section can be mis-measured by up to $\pm 30\%$.

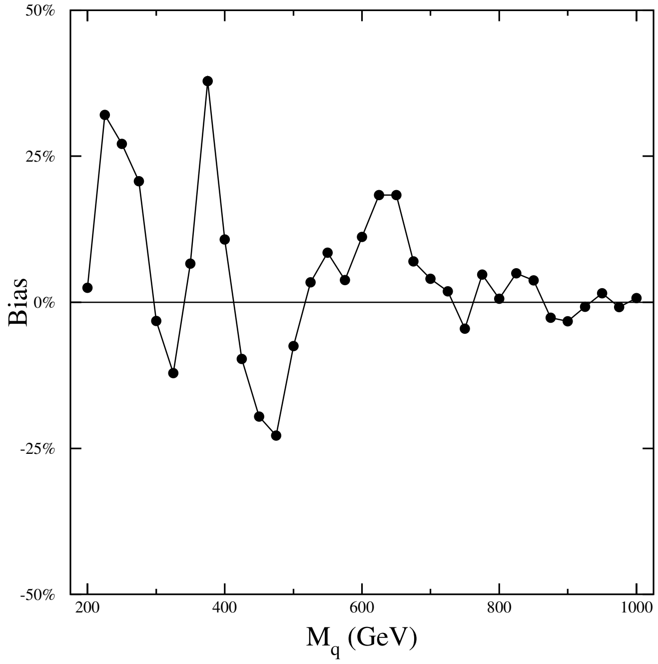

FIG. 23. The Bias in the ansatx function method.

Finally, $\sigma_{95\%}$ is compared with the predicted production cross section of an excited quark to test the statistical power of the ansatz function method, this comparison is shown in Figure 24. Although the ansatz function method produces a similar mass constraint to the Baysian method it does not produce as effective cross section limits over the entire mass range.

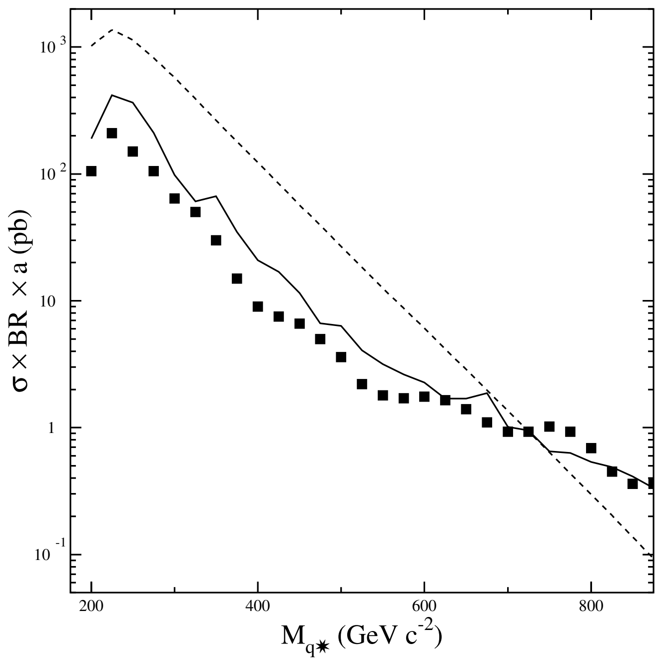

FIG. 24. The 95% CL on the production cross section ($\sigma_{95\%}$) for the q^* (solid line) compared with the predicted cross section (dashed line) for the ansatz function method.